Geographical Distribution and Inter-Seasonal Variability of Tropical Deep-Convection: UARS MLS Observations and Analyses

J. H. Jiang[1], B. Wang[2], K. Goya[3], K. Hocke[*], S. D. Eckermann[4], J. Ma[5], D. L. Wu[1], and W. G. Read[1]

[1] Jet Propulsion Laboratory, California Institute of Technology, Pasadena, CO, U.S.A
[2] Department of Meteorology, University of Hawaii, Honolulu, Hawaii, U.S.A
[3] Geophysical Fluid Dynamics Laboratory, Kyushu University, Fukuoka-shi, Japan
[4] Naval Research Laboratory, Code 7646, Washington DC, U.S.A.
[5] Computational Physics Inc., Springfield, Virginia, U.S.A.
[*] See Acknowledgement

Submitted to JGR-Atmosphere

Short title: Satellite observation of tropical convection

Key Words: climate, convective processes, dynamics, gravity waves, stratosphere-troposphere interaction, and tropical meteorology

Abstract

Tropical deep-convection and its dynamical effect on the tropopause and stratosphere are investigated using a suite of data from the Upper Atmospheric Research Satellite (UARS) Microwave Limb Sounder (MLS), including upper tropospheric humidity, cloud radiance, and gravity wave measurements. For this purpose, geographical distributions of temperature, water vapor and cloudiness in the tropical tropopause layer (TTL) are compared with corresponding maps of gravity wave variance in the stratosphere. In addition, ECMWF global wind divergent and velocity potential fields as well as CMAP rainfall data are analyzed to help pin-point the location of deep-convection. We found that high-altitude clouds near the bottom of TTL (~147 hPa) are usually surrounded by high humidity air, and their spatial pattern and seasonal variability are closely associated with regions of vigorous summertime deep-convection. Upward propagating gravity waves generated by these convections are shifted poleward by prevailing stratospheric winds. We estimate that tropical deep-convections lift ~ 5% of the cloud tops to altitudes above ~100 hPa, and that most of these extreme deep-convections occur in the Western Pacific and Indian monsoon regions. The maximum cloudiness in the TTL occurs during the Southern Hemisphere summer when the tropopause is highest and coldest. Low temperature regions in the TTL are associated with, but often drift away from the center of deep-convection. Regions of water vapor maximum near the bottom of TTL are located directly above the deep-convections, but this moisture behavior is somewhat reversed at the top of the TTL and seems to also locate near the deep-convection centers. The integrated picture derived from this study imply that convective scale motions might be important in affecting short-term dehydration processes in the TTL. Our results also suggest that the spatial organization and temporal development of tropical convective systems will be better monitored with the follow-on Earth Observing System (EOS) Aura satellite instruments, and lead to improved understanding of the complex interaction of tropical convection with large-scale dynamic and thermodynamic conditions.

1. Introduction

Convection is formed from convective warming of mid-troposphere initiated by a surface warming [*Holton*, 1992]. Deep convection is a more vertically developed and localized convection event that is characterized by rapid injection of surface air near or through the tropopause. Cloud or cloud systems form by condensation in these convecting air masses near the tropics are the primary mechanism by which solar heat moves from the ocean upward into the free troposphere, where it can be transported poleward and eventually emitted to space. In the process, these great engines of the global climate produce precipitation and drive the global-scale circulation. The combined effect of these convective systems and the large-scale circulations with which they interact determines the cloudiness, moisture, and temperature structure of tropical troposphere, which in turn plays a central role in determining the global climate.

Water vapor transport across the tropical tropopause

Tropical deep convection is also the main source of water vapor for the upper troposphere. This upper-tropospheric humidity (UTH) plays an important role in maintaining the natural greenhouse effect in the atmosphere. The maximum level of neutral buoyancy of tropical deep convection is around *14 km* (~150 hPa) [*Highwood and Hoskins*, 1998], which is the level of convective equilibrium of the tropical troposphere. Rapid ascending air masses generated by deep convection can overshoot this convective equilibrium level and reach as high as ~*18 km* (~70 hPa) [*Sherwood and Dessler*, 2001], which is near the level of radiative equilibrium of the stratosphere (i.e., the lowermost stratosphere). The region between the tropospheric convective equilibrium and the stratospheric radiative equilibrium near the tropics is referred to as tropical tropopause layer (TTL), and is understood as the region of gradual transition from the troposphere to stratosphere.

The physical processes occurring in the TTL are of great interest, because the observed low concentration of stratospheric water vapor can not be explained unless tropical tropospheric air entering the stratosphere through the TTL is dehydrated to stratospheric abundance of *~4 ppmv* from *~13-20 ppmv* [*Brewer*, 1949; *Dessler and Kim*, 1999; *Holton and Gettelman*, 2001]. The amount of water vapor in the stratosphere is important because it can affect stratospheric chemistry and radiative balance [*Kirk-Davidoff* et al, 1999; *Forster and Shine*, 1999]. Since the traditional "freeze drying" mechanism at the zonal mean TTL can not explain the stratosphere dehydration to the observed water vapor mixing ratio, *Newell and Gould-Stewart* [1981] proposed a "stratospheric fountain" hypothesis, that is, the tropical tropospheric air enters the stratosphere preferentially in "cold" areas where the tropical tropopause temperatures are below their annual and longitudinal mean values. The "fountain" region is mainly over the Western Pacific, with a little variation with season. However, later studies suggest that the Western Pacific can actually be an area with net subsidence at the tropopause [*Sherwood*, 2000; *Gettelman et al*., 2000]. *Holton and Gettelman*, [2001] suggested that this paradox can be resolved by assuming that horizontal transport through a "cold" region (e.g., the Western Pacific) causes air parcels that reach the tropopause at other longitudes to be dehydrated to the very low saturation mixing ratios having characteristic of the "cold" region. This hypothesis implies that tropopause temperature variations in areas other than the Western Pacific also affect the entry value of water vapor mixing ratio from the troposphere into the stratosphere.

Another hypothesized mode of dehydration of air entering the stratosphere involves deep convection overshooting in the TTL. As discussed in *Johnston and Solomon* [1979], such convection would result overshooting airmasses adiabatically cool to much lower temperatures than surrounding airs in the TTL. Growth of ice particles in the convecting air mass followed by sedimentation could effectively remove much of the water in the process. This dehydration by overshooting convection is used by *Sherwood and Dessler* [2000; 2001] to model the stratospheric dehydration. An important question to test this hypothesis is how frequently, and where the deep-convection penetrates the tropopause. In the past decade, several observational efforts have been made to map overshooting convection over the land or water near the tropics [e.g. *Hendon and Woodberry*, 1993; *Mapes and Houze*, 1993; *Liu et al.*, 1995; *Hall and Vonder Harr*, 1999; *Roca and Ramanathan*, 2000; and *Soden*, 2000]. However, the relative importance of convective overshooting in the control of stratospheric humidity is still an open question.

On the other hand, observational proof of the *Holton and Gettelman's* [2001] "cold-trap" hypothesis requires investigation of spatial and temporal variation of cold anomalies in the TTL and their relation to regions of low water mixing ratio. On a short time-scale (hours to days), several observations suggest that the tropopause cold region is correlated with strong convection. For example, *Johnson and Kriete* [1982] found a ~ *6 K* cold anomaly near the tropical tropopause associated with local deep-convection; *Teitelbaum et al.* [2000] found a simultaneous response of the tropical cold tropopause region to an incidence of deep-convection. Recently, *Clark et al.* [2001] examined the 5-day evolution of MLS 68 hPa water vapor features during the dry phase of the atmospheric "tape recorder" [*Mote et al.*, 1996], and found they could not be explained by horizontal advection. On longer time-scales (weeks to months), tropopause cold regions are affected by Kelvin waves [*Tsuda et al.,* 1994a; *Boehm and Verlinde*, 2000; *Holton et al*, 2001]. The annual variation of the zonal TTL is mainly driven by extra-tropical stratospheric winds forcing, but some of the cold regional tropopause temperature anomalies can be seen to be due to the response of the atmosphere to tropospheric diabatic heating [*Highwood and Hoskins*, 1998]. At even longer time scales (several years), the tropical cold tropopause region may be affected by ENSO [*Randel et al*., 2000], volcanic eruption, solar cycle, and climate change. For example, a cooling trend of tropical cold tropopause region has been reported by *Zhou et al*., [2001] from 1973-1998 sounding data. Most recently, *Read et al.* [2003] investigated inter-annual evolution of water vapor in the TTL measured by MLS. While not conclusively ruling out the importance of convective dehydration, their data show evidence of slow ascent of tropical water into the TTL between 12°S-12°N zonal averages, and the result appears to be consistent with the model employing large scale transport and freeze-drying in the cold region over a 1.5-year period of 1991-93.

Gravity waves radiated from deep-convection

Another way to study the characteristics of convection motion is to investigate the gravity waves (GWs) radiated from deep-convection. *Fovell et al.* [1992] studied generation mechanism and vertical propagation of GWs excited by a squall line using a 2D non-hydrostatic model. It is shown that the short period (*18-24 mins*) of dominant GWs generated by the squall line correspond to the period of the mechanical upward wind due to the moist convection. By comparing the result of the squall line case to the results of mechanically dry convection case, it is concluded that mechanical forcing driven by convection is the main factor for GWs generation by the squall line rather than thermal effects. *Alexander et al.* [1995] further investigated the excitation mechanisms of

GWs due to the convective storms using the customized 2-D numerical model of *Fovell et al*. [1992]. Their study reports that three properties of a storm could govern the GWs generation mechanism, 1) depth of the diabatic heating layer, 2) oscillation frequency of the main updraft, and 3) the storm propagation speed. Independently, *Goya and Miyahara* [1998, 1999] used their 2D non-hydrostatic model to simulate the generation of GWs by tropospheric dry convections and their vertical propagation and evolution throughout the middle atmosphere. Their study focused on the generation and breaking of primary and secondary GWs above the convection sources. Though the primary source of GWs in their study is dry convection, they also show that in most moist convection, the period of the dominant GWs corresponds to the dominant period of vertical wind due to the dry convection. Therefore they suggested that mechanical oscillation in the convections, no matter moist or dry, is the most essential role for GWs generation. Moreover, they argued that the background wind above the convection source determined whether the oscillation of turbulence in the convection could excite internal GWs or external GWs above the convection. Using a customized 2D model as *Fovell et al*. [1992] and *Alexander et al*. [1995], *Holton and Alexander* [1999] also simulated dynamical behavior of GWs generated by a convective storm to investigate primary GW propagation and breaking in the middle atmosphere. *Lane et al.* [2001] especially focused on GWs generation mechanism due to deep convections with horizontal size on the order of 100 km. Their study shows that a nonlinear effect due to the advection term of the Navier-Stokes equations dominate the GWs generation rather than the latent heating term and eddy diffusion term. They also emphasize that oscillation of upward wind due to deep convection generates the main GWs at level of neutral buoyancy around the top of deep convection [*Vadas et al*., 2003].

The characterization of differences between convection over land and convection over sea is another topic of research. Land and ocean have different specific heats. Tropospheric convection occurs when a strong inversion layer of temperature appears. Land might play a role in heating the air and producing a temperature inversion layer in the lower troposphere in the daytime and thus affect the strength of the convection. However, future studies using more detailed observation and modeling will be required to distinguish between the GWs generated by oceanic convection from GWs generated by topographical convection.

Purpose of this study

In this paper, we investigate the convective scale perturbations in the TTL and their potential influence to stratospheric dehydration by studying the geographical distribution and temporal variation of tropical deep-convection using a unique suite of data from UARS MLS. This suite includes water vapor, cloud radiance, and GW measurements. We focus on possible links between the low water vapor regions, low temperature regions, high-altitude clouds, and their relations to the convectively generated GWs. A brief description of the MLS data used in this study is given in section 2. The findings and analyses from these MLS observations are presented in two parts in section 3: one part focuses on the distribution and variation of water vapor, temperature and cloudiness in the TTL; another focuses on the GWs in the stratosphere and how they relate to the former quantities in tropical deep-convection events. Some preliminary modeling and other data support are presented in section 4. Concluding remarks are given in section 5.

2. MLS measurements

Launched on September 12, 1991, the UARS MLS measured limb atmospheric thermal radiation at 63, 183, and 203 GHz. Detailed descriptions of the orbital coverage, mission operations and the major measurements of UARS MLS are given by [*Waters et al.*, 1999 and *Livesey et al*., 2003]. The following are brief descriptions of MLS products related to this study.

MLS upper tropospheric humidity (UTH) products

Two upper-tropospheric humidity (UTH) products have been developed by the MLS science team. V4.9 [*Read, et al*., 2001], derived from UARS 203-GHz radiances, provides water vapor mixing ratio and relative humidity with respect to ice from 467 to 147 hPa. More recently, V7.02 [*Read et al*., 2003] has been developed to fill the gap between 147 hPa and the 100 hPa bottom of the 183-GHz stratospheric water vapor product V0104 [*Pumphrey*, 1999]. The V7.02 data set is available from October 1991 to April 1993, and these combined products give a continuous profile from 464 to 0.1 hPa with *~3-4 km* vertical resolution. The estimated precision and accuracy for the V7.02 water vapor are respectively *~0.1 ppmv* and *~1 ppmv* at 100 hPa.

MLS cloud radiance measurements

MLS cloud radiances are deduced from the UARS MLS 203 GHz radiances. As described in *Livesey and Wu* [1999] and *Wu and Jiang* [2002b], measured clear-sky 203-GHz radiances profiles as a function of scan angle are tightly clustered within bands given by the limits of water vapor variability. A simulated radiance profile using a clear-sky radiative transfer model [*Wu and Jiang* 2002b], with *110%* relative humidity (super-saturation in water vapor) throughout troposphere provides a limiting case for radiances which can be explained by water vapor variability in the absence of clouds. Clouds at high tangent heights (higher than ~*12 km*) produce radiances that are warmer than the *110%* saturation limit and could be recognized and flagged. Similarly, clouds at low tangent heights (lower than ~*6 km*) may produce perturbations cold enough to be below the *110%* saturation limit and be detected. Such simulations using a cloudy-sky radiative transfer model are described by *Wu and Jiang* [2002b] and *Wu et al*. [2003]. In some cases, the UARS MLS measured cloudy-sky radiances at 203-GHz can be ~*20 K* larger than the clear-sky limit at high tangent highs or as low as < *120 K* below the clear-sky limit at low tangent heights. In the middle tangent range between ~*7* and ~*11 km*, clear- and cloudy-sky radiances are not so easily distinguishable. We define the cloud-induced radiance (*K*), or simply *cloud-radiance*, as the difference between the cloudy-sky radiance and the clear-sky saturated-humidity limit at each tangent height.

In this paper, we use cloud radiances at high tangent heights of ~*14 km* and above (i.e. $\leq$147 hPa). At these tangent-heights, the majority of the radiances observed by MLS originate from a region around the tangent-point, which is the lowest point along a limb path. Only high-altitude clouds having cloud-tops reaching within ~ ±*1.5 km* of that level can affect measured radiances. In other words, the 147 hPa cloud radiances are due to the presence of *high-clouds* that having altitude of ~*14 km* or higher. The model uncertainly is ~ *2-3 K* at 100 hPa near the tropics. In this paper, we set the threshold of positively flag a cloud signal as > *3 K* in cloud-radiance. The *cloudiness* (*%*), or the cloud occurrence frequency, is defined as the ratio of total clouds flagged over the total number of samples.

MLS gravity wave variances

The MLS gravity wave (GW) variance is computed from the UARS MLS 63 GHz saturated limb radiance measurements at the bottom of each scan. Detailed descriptions of MLS GW radiance calculations and the recent improvements are given by *Wu and*

Waters, [1996a,b], and *Jiang et al*., [2003a,b]. These GW variances are available at 8 altitudes (*28, 33, 38, 43, 48, 53, 61,* and *80 km*) and are contributed mostly by waves of vertical wavelengths *>10 km* and horizontal wavelength of *~50-150 km*. Recent studies using the MLS GW variances (some combined with model simulations) have related many of these GWs to the topography [*Jiang et al*., 2002, 2003a,b], convection [*McLandress et al*., 2000] and possible jet-stream origins [*Jiang and Wu*, 2001].

In this study, we use the improved 4-point MLS limb-scan GW variances described by *Jiang et al*. [2003a,b]. We focus on the GW activities in tropical and sub-tropical regions and compare them with the MLS UTH and cloud radiance measurements.

3. MLS observations and analyses

To understand the distribution of tropical convection and its relation to the transport of air into the TTL, we first investigate the cloudiness, temperature and water vapor fields near the bottom (147 hPa), the midway (100 hPa) and the top (68 hPa) of TTL.

Cloudiness, cold tropopause region, and water vapor distributions in the TTL

The black contour lines in Figure 1a,b,c show the distribution of TTL cloud occurrence frequency, or cloudiness (*%*), as indicated on the contour-labels. The MLS 203-GHz cloud radiance measurement is most sensitive to clouds having ice water content greater than *~0.005 g/m3* [*Wu and Jiang*, 2002b]. These dense high-altitude clouds seen by MLS are most likely lifted by deep-convection events (rather than thin cirrus which have smaller particle sizes) and their distribution is highly correlated with locations of vigorous convection activities. Regions of lowest TTL temperature (as indicated in the figure caption) are filled by the blue-color. The green-colored areas are the regions with minimum V7.02 water vapor mixing ratio as indicated in the figure caption. Note at 147 hPa, the green color filled most of the region but left a white area near the tropics that shows the region of maximum water vapor concentration. Tropical wind profiles for the major convection centers are also plotted at the bottom panels of Figure 1a,b,c.

[Insert Figure 1 here]

***December-March* (*Figure 1a, and 1b*)**

Near the bottom of TTL at 147 hPa, there is a positive correlation between the centers of moisture maximum and the centers of high cloudiness. This correlation indicates cloud formation and rapid vertical transport of boundary layer water vapor in the deep-convection. The region of lowest temperature at this altitude mainly resides from the south Indian Ocean to the Western Pacific, and its center is closely correlated to the bulk of high cloudiness area. Note at this altitude over the Western Pacific, the tropical winds are westward directed (slightly northwestward), and the low temperature regions seem to locate at slightly downwind from the convection center.

At the higher altitude of 100 hPa, most low water vapor region (filled by green-color) is located northward of the tropical convection zone. The regions of lowest temperature (filled by blue-color) are somewhat correlated with convection centers, but seem to also shift slightly northward relative to the high-cloudy area. Such a displacement is similar to that seen in HALOE data by *Randel et al.* [2001].

Near the top of TTL at 68 hPa altitude, the cloudiness frequency is largely reduced to a little above *2%* and seems to mostly locate over the Western Pacific. At this altitude and above, the winds are mostly easterly (i.e. westward) jets. The low-temperature spots and a low-water vapor region over the Western Pacific appear somewhat influenced by this wind pattern. Comparing the values of cloudiness at the bottom of TTL to those at the top, we estimate that about *5%* of clouds that appeared at 147 hPa are lofted to as high as 68 hPa, and these very high altitude clouds are located mostly over the Western Pacific Ocean. Some caution should be taken in interpreting this as evidence that the deep-convection penetrates to 68 hPa because the vertical smearing of the MLS data is about *3-4 km*. Nevertheless, comparing to Western Pacific, the lack of 68 hPa clouds over the African and South American continental regions might suggest that oceanic deep-convection (such as those over the Western Pacific) is most capable of over-shooting the tropical tropopause.

It is also worth noting that the moisture behavior at 147 hPa is the inverse to that at 68 hPa, which arguably imply a dehydration process occurs near the top of TTL above the convective sources. The fact that the centers of minimum water vapor and temperature at 68 hPa is located at slightly downwind of the deep-convections, is (although arguably) also predicted by the 'convective-overshooting' dehydration hypothesis.

Also to note is that tropics of December-March of 1991/92 (Figure 1a) appear to have more clouds in the TTL than they do in December-March of 1992/93 (Figure 1b), a possible indication that there was more moisture entering the upper-troposphere to form clouds in the 1991/92 northern hemispheric (NH) winter/early spring than in the following year. Plausible reasons behind this include the impact of Mt. Pinatubo aerosol on cirrus clouds formation [*Liu and Penner*, 2002; *Lohmann et al.*, 2003], and the influence of ENSO to tropical climate [*Massie et al.*, 2000; *Jensen et al*. 1996].

***July-September* (*Figure 1c*)**

During NH summer to early fall (Figure 1c), two major convective centers lift high moisture and cloudiness into the TTL. The largest one that stretches from Tibet/South China to South/Southeast Asia is possibly related to the Indian monsoon. The winds at ~147 hPa (and lower altitudes) over Tibet blow eastward (slightly southeastward), while the winds over South Asia are westward (slightly southwestward). The low temperature region at this altitude mostly occurs near the southern edge of this huge anti-cyclonic wind pattern (see the red arrows) at 147 to 100hPa. An estimated *~5%* of the clouds at 147 hPa reach as high as 68 hPa, where the winds become mostly westward. The region of minimum water vapor at the top of TTL (68hPa) appears in the equatorial zone mostly over the Indian ocean to Western Pacific, while the minimum temperature regions are scattered around west to south of the India monsoon. The central American monsoon is much smaller in scale but is clearly correlated to a small "cold-spot" at the 147hPa bottom of TTL.

It is worth to note that the two regions of maximum moisture at both 147hPa and 100hPa are associated with the high cloudiness over Indian and American monsoons. This moisture behavior is not reversed at the top of TTL as it does during the Dec-Mar season, suggesting that convections over the land masses might be acting to moisten the air in the TTL, rather than dehydrate it.

The new V7.02 water vapor data that is used to plot the maps in Figure 1 is not available for summer of 1993, but our analyses found the low-temperature areas (not shown here) distributed in 1993 summer are more or less the same as those in the 1992 summer. Also to note is that there is seem to have less TTL cloudiness during the NH summer than during the NH winter/SH summer (compare the values labeled on the cloudiness contour). This indicates maximum cloudiness in the TTL occurs during the NH winters, or Southern Hemisphere (SH) summers, when the tropopause is highest and coldest. (Also see Figure 8 in the later section for comparison between time-series of cloudiness during SH and NH summers).

Stratospheric gravity waves above the TTL

While more attention has been paid to the temperature and moisture in the studies of TTL dehydration, clear correlation between deep-convection and enhanced GW activity has been observed, particularly in tropics [e.g. *Karoly et al.*, 1996; *Tsuda et al.*, 1994b, 2000; *Alexander et al.*, 2000; *Preusse et al.*, 2001]. In some cases, GWs associated with convection weather can feed back to modify or organize severe deep-convection and precipitation [Koch and Siedlarz, 1999]. Thus knowledge of how GWs propagate upward above the tropopause in background winds, and how their distribution and time evolution linked to climate conditions can yield rich information about convective activities near the tropics.

Effect of the background winds

Let's first look at how GWs propagate upward in the background winds. GWs generated by deep-convection usually have short periods and thus the linear theory can be applied [*Salby*, 1996]. To access the influence of background winds on the vertically propagating GWs, the following dispersion relationship derived from a non-hydrostatic, compressible, 2-D fluid equation system is useful when the Doppler effect is taking into account:

$$m^2 = \frac{N^2}{(\bar{u}-c)^2} + \frac{k^2(\bar{u}-c)^2}{c_s^2} - k^2 \qquad (1)$$

where k denotes horizontal wavenumber, m vertical wavenumber, $\bar{u}$ zonal mean wind velocity , c horizontal phase velocity, c_s sound velocity and N buoyant frequency. For $m^2 > 0$, the solutions for the basic equations become a sinusoidal form in the vertical direction, and are referred to as internal. An amplitude of the GW increases with ratio of $exp(z/2H)$, where H is the scale height. *For* $m^2 = -m'^2 < 0$, the solutions become $exp(-m'z)$ in the vertical direction and the phase becomes constant with height, and are referred to as external. Even though their energy decreases, external waves in the range $1/2H > m'$ amplify upward like $exp[(1/2H - m')z]$ due to stratification of the background atmosphere. On the other hand, they damp upward in the range $1/2H < m'$.

Environmental conditions determine N, c_s, and $\bar{u}$. Physical aspects of the convections control GWs spatially and temporally (as mentioned in section 1). Thus k and c are determined by the convective source. Finally, the vertical wavenumber m may be determined. According to equation (1), it is found that the static stability N^2 mainly contributes to the positive part of m^2. Since k^2 reduces m^2, GWs with short horizontal wavelength cannot propagate vertically for a particular k. Vertical propagation is strongly controlled by the intrinsic phase velocity $c - \bar{u}$. Thus when GWs generated by convections vertically propagating through the shear wind zone, filtering due to the background wind happens. For example, when $\bar{u} \sim 40\text{-}50\ m/s$, assuming $N \sim 0.02\ rad/s$, the vertical wavelength of GW can be estimated as $\lambda_z \sim 13\text{-}16\ km$, which is within the MLS filter range. Conversely, if the value of $\bar{u}$ is small or negative it could result in the GWs having too short a vertical wavelength to be visible by MLS.

[Insert Figure 2 here]

The effect of filtering by the background wind, as described above, can be best illustrated by Figure 2, which shows measured MLS zonal mean GW variances in January 1992-94 (left) and July 1992-94 (right) in comparison with CIRA zonal wind climatology [*Fleming, et al.*, 1990]. The GW variances exhibits a slight tiltness similar to the stratospheric and mesospheric jets, which are tilted southward with height in SH summer (January), and tilted northward with height in NH summer (July). In January, at latitudes of ~50°N to ~70°N, orographic mountain waves [*Jiang et al.*, 2003a,b] and jetstream-induced waves are the major GWs seen by MLS; at latitudes of ~5°S to ~25°S, convection-induced GWs [*McLandress et al*., 2000] are the primary sources. In July, the wave sources at latitudes of ~40°S to 70°S are likely the combination of mountain waves from South Andes, Drake Passage, and the Antarctic rim [*Jiang et al*., 2002, *Wu and Jiang*, 2002a, *Eckermann et al*., 2003]; at latitudes around 25°N, the GW sources are primarily from subtropical deep convection. The lowest zonal GW variances are observed around the zero wind lines above the tropics.

[Inset Figure 3 here]

GW variance maps

We now pay our attention to the distribution of GWs above the TTL. Because of background wind filtering effect discussed above, the center of maximum GWs at higher altitude shift southward in SH summer and northward in NH summer relative to GWs at lower altitude, as shown by two examples in Figure 3, in which GWs at *28 km* (black contour-lines) and at *38 km* (color-filled contours) are both plotted. In summer hemispheres, the background stratospheric winds are usually greater than *~30 m/s* at altitudes ≥ *38 km* above the subtropical convection zones, thus GW is mainly detectable by MLS at this height (*~38 km*) and above (see Figure 2). Occasionally, MLS also detects the GW signals as low as *~28 km*, such as during December-March of 1991-92 (Figure 3 top panel) and June-September of 1994 (Figure 3 bottom panel). In other years/seasons, e.g. December-March of 1992-93, GWs at 28 km are mostly undetectable by MLS due to unfavorable wind conditions. Thus, to compare GW distribution with TTL cloudiness map, we will focus on MLS GW maps at 38 km, where the GW is detectable for all 1991-94 NH winters and summers. Figure 4a,b show the maps of such comparison. In these maps, GWs are shown by color-filled contours, where the V4.9 relative humidity with respect to ice (*RHi*) at 147 hPa (shown as the black contour-lines) and cloudiness (*%*), also at 147 hPa (shown as the white contour-lines) are over-plotted. (The reason that we use the V4.9 *RHi* in these maps, other than the V702 is that V4.9 data at 147 hPa cover longer time period so we can use them to compare with the MLS GW data). To best illustrate these maps, only contour values with *RHi* $\geq$ *90%* and *cloudiness* $\geq$ *20%* for December-March and *RHi* $\geq$ *80%* and *cloudiness* $\geq$ *15%* for June-September are shown.

[Insert Figure 4 here]

The most obvious feature in Figure 4 is that the maximum GW activity areas, due to the background wind filtering effect, are located poleward relative to the center of cloudiness regions. Also, the center of TTL cloudiness are drifted to western (or downwind) of the active GW regions, especially in SH summers. Nevertheless, MLS observations show that during the NH winter and early spring (December to March), strong GW activities seem to correlate with the tropospheric deep convection zones in the tropics (see color-filled contours in Figure 4a). These activities are centered at Southern Africa, Western Pacific, and South America. In previous analyses with MLS data [e.g. *Wu and Waters* 1996b, *McLandress et al.*, 2000], the variances were smoothed over a large area to improve GW signal-to-noise ratios. As a result, it was only possible to visualize planetary-scale features. With the recently improved 4-point limb-scan variances [*Jiang et al.*, 2003a] that are used in this study, more details on convection-induced GWs can be seen. Some of the convection-related GWs may be correlated with topographic features including small islands in the south Pacific. The storm systems over oceans generally produce weaker GW variances compared to those hitting the east side of land masses. During the NH summer to early fall (June-September) the GW variances show strong wave activities over the subtropics of the northern hemisphere, including major wave activities at Northern Africa, South Asia, and Central America (see color-filled contours in Figure 4b).

Also, it is obvious that there is a good correlation between the cloudy region and high *RHi* area (both in the Figure 4a and 4b), in the sense that water vapor more frequently condenses to form clouds in air parcels with high relative humidity (*≥ 100%*).

MLS inferred wave propagating direction

The GW variance maps shown in Figure 3 and 4 are averaged over MLS north-looking ascending (NA) and south-looking descending (SD) orbits. (Detailed description of different MLS orbits and observation models can be found in *Jiang et al*., [2003a,b], and in *McLandress et al*., [2000], and are not discussed here). This is because the MLS GW variances are very sensitive to the wave propagation direction [*Jiang and Wu*, 2001; *Jiang et al*. 2003a,b]. For the convective cases, we found that variances are much stronger when observed either on NA or SD orbits than they are when measured on north-looking descending (ND) or south-looking ascending (SA) orbits (see examples in Figure 5). In tropics and low latitudes, the MLS line-of-sight (LOS) is mostly pointing toward the west direction and is scanning from top to surface when it is in the NA or SD observing modes. The fact that much stronger GW signals observed from these two observing modes imply that vertically, a downward propagating wave front must be tilted toward east (as shown in Figure 6). (This is different with the wave front travel direction of winter-time orographic "mountain waves" described in *Jiang et al*., [2003a,b]. The MLS observed orographic wave variances are strong in ND and SA modes, which imply the wave-front is tilted toward the west). In the subtropics of both north and south summer hemispheres, the stratospheric jets are predominantly westward winds. As illustrated in Figure 6, the propagation direction of convection generated gravity waves observed by MLS is tilted in such way that the horizontal component of the wave vector $\mathbf{k_h}$ is opposite to the wind vector **U**. The other "half" of the waves with $\mathbf{k_h}$ traveling in the same direction as **U** is "dead", or "filtered out" in the background winds. In other words, the GWs observed by MLS are dominated mostly by the downward-phase propagating waves having horizontal phase-velocities opposite to the stratospheric jet-streams. This is in agreement with the numerical model simulations [e.g. *Goya*, 1998; *Goya and Miyahara*, 1998; and *Lane et al.*, 2001], which show that vertical propagating GWs generated by convection expand to a fanlike region, and spread horizontally with height in the direction facing the background wind. NA and SD MLS viewing direction, depicted as direction B in figure 2, is favorable for resolving this wave pattern generated by convection because it intercepts the wave roughly parallel to its tilted wave fronts.

[Insert Figure 5 and Figure 6 here]

MLS observed vertical growth of GWs

Figure 7 show mean vertical profiles of GW variances normalized by mean radiance brightness temperatures, derived from 3 years of limb-scan measurements in above the major SH and NH summer convection centers in the subtropics. These profiles show that the convection generated GWs grow exponentially when propagates through the stratosphere. This is consistent with earlier zonal mean profiles show in Figure 2. Below ~ *50 km*, the growth rates are closely following the nondissipating rate ~ $\exp\left(\int dz/H\right)$, where H ~ *7 km* is the scale height [*Fritts and VanZandt*, 1993]. At altitudes above ~ *50 km*, the growth rate becomes smaller, possibly due to wave dissipation/saturation [*Wu*, 2001], or wind-modulated apparent "saturation" in MLS variances [*Alexander*, 1998].

[Insert Figure 7 here]

Seasonal and inter-annual variation

As to the seasonal and inter-annul variability in the tropics, Gettelman et al., [2000] reported a declining trend of MLS V4.9 relative humidity (and therefore cloudiness) in 1991-94 time period. They have shown a minimum relative humidity but maximum temperature between 147-215 hPa in 1994, as well as a shallow maximum of water vapor mixing ratio at the same level. Although several possible mechanisms that could cause this anti-correlation of temperature and cloudiness during this time scale are discussed (e.g. Pinatubo eruption and El Nino and La Nino events), there is no firm conclusion to this question.

In previous discussions, we have shown that deep-convections are highly localized events. The seasonal and inter-annual evolution of these localized convections can be assessed by time-series of 30-day running window mean of TTL cloudiness and convection-generated GW variances (also 30-day running window mean), as shown in Figure 8. There is a somewhat decreasing trend of the 100 hPa cloudiness in 1991-1994, for all three NH wintertime/SH summertime convection-active regions (Southern Africa, Western Pacific and South America). However, there is little evidence of decreasing in frequency and strength of the tropical/sub-tropical deep-convections found in the 38 km GW variances in 1991-94, although we can not completely rule out such possibility since GWs strength also determined by the background winds, and further modeling studies are required. For the two dominant convection sources in NH summer (Indian monsoon and American monsoon regions), the deep-convections in the Indian monsoon area seem to generate more high cloud amount in the TTL and stronger GW variances in the stratosphere. However, compare the three NH summers in 1992-94, there is no clear decreasing nor increasing trends.

[Insert Figure 8 here]

It is also interesting to note that in SH summer, convections over large landmass (i.e. Southern Africa and South America) seem to generate stronger GWs compared to those GWs over the ocean (e.g. Western Pacific). However, convection over the ocean clearly has more updraft potentials to lift cloud tops into the TTL (e.g. above Western Pacific). In NH summer, convection from the larger India/South China landmass both seem to generate stronger GWs and lifts more clouds into the TTL compared to that from the smaller Central American landmass.

4. Preliminary MWFM simulation and ECMWF analyses

Topography disturbances simulated by MWFM

In order to see whether some of the TTL disturbances and stratospheric GWs are actually topographically forced mountain waves (MWs), the Naval Research Laboratory Mountain Wave Forecast Model version 2.1 (MWFM 2.1) is used to simulate stratospheric temperature perturbations produced by upward propagating orographic waves. The MWFM 2.1 is described in detail by *Jiang et al*. [2003b] and *Eckermann et al*. [2003]; a brief description is given here. MWFM blows atmospheric winds over digital representations of the Earth's major topographical features and calculates a spectrum of forced mountain waves. The model simulates subsequent propagation of these waves according to vertical profiles of winds and temperatures, and keeps track of the waves' amplitudes along the way [*Broutman et al.,* 2001]. The background temperature and wind fields are taken from the United Kingdom Meteorological Office (UKMO) assimilated meteorological data. The ray equation in MWFM 2.1 is governed by a non-hydrostatic dispersion relation with rotation and density scale height according to *Marks and Eckermann* [1995]. The MWFM simulations in this study are unfiltered according to MLS weighting function.

[Insert Figure 9 here]

Figure 9 illustrates the simulated MW activities at 5 hPa (~*37 km*) for both SH summer (left panel) and NH summer (right panel). In both the winter and summer cases, MWFM results show sub-tropical orographic wave activities over the mountain ridges of northern India, Middle East, and Mexico. However, modeling studies using a sophisticated MLS filter [*Jiang et al.*, 2003b] indicated that due to unfavorable stratospheric wind conditions over the northern subtropics during SH summer, orographic waves over these regions have "wind-filtered" vertical wavelengths of < *10 km* and thus are unlikely to be seen by the MLS. During the NH summer, however, substantial wave activities over northeast Africa and Mexico might be seen by MLS. A recent study by *Goya* [1998] using a 2-D non-hydrostatic model shows that stratospheric GWs generated by deep-convections could have vertical wavelength of >*13 km*, which is within the MLS filter range. Thus, with the MWs being ruled out, MLS measured GW activities in tropical and sub-tropical regions during the SH summer/NH winter (December-March) indicate strong convective activities in these regions. During the NH summer (July-September), subtropical wave turbulences seen by MLS might be mixed with both convection and topography generated GWs.

Convective perturbations from ECMWF wind and CMAP rainfall analyses

From the MLS observations of stratospheric GWs and upper-troposphere cloudiness described in the previous sections, it is obvious that deep convection near the tropics seem to occur in preferred regions. To see if the wind fields and rainfall pattern agrees with the MLS data, we show in Figure 10 the maps of 150 hPa monthly mean wind (top panels), velocity potential and divergent wind (middle panels) derived from the European Centre for Medium-Range Weather Forecasts (ECMWF) gridded global analysis. The data are averaged for January 1992-94 (left panels) and July 1992-94 (right panels) to illustrate both SH and NH summers. Also shown at the lower panel in Figure 9 is the monthly mean precipitation derived from the Climate prediction center Merged Analysis of Precipitation (CMAP) for the same period. The CMAP blends station rain observations and five different types of satellite products to estimate global precipitations [*Huffman, et al*., 1997; *Xie and Arkin*, 1997]. The CMAP patterns in the tropics are quite similar to maps of outgoing longwave radiation (OLR) and can be used to pin-point regions of deep-convection [*Wang*, 1994].

[Insert Figure 10 here]

The January wind field reveals the dominance of strong westerlies over subtropics both north and south of the equator. In deep tropics, the easterlies associated with SH summertime monsoon prevail over the maritime continent, western Pacific, and equatorial Africa; meanwhile westerlies occur in the eastern Pacific and Atlantic Oceans (the "westerly duct"). The velocity potential and rainfall configurations are asymmetric about the equator. The SH is dominated by three major divergent centers over central to southern Africa, Western Pacific and South America. The SH summertime deep-convection is most pronounced over Indonesian seas and the Western Pacific. The upper-level divergent outflows from regions of heavy rains penetrate as far north as east China and Japan. This corresponds to the local Hadley circulation during the SH summer. The CMAP rainfall pattern indicates convections occur across 10°N to 20°S latitudes, however, maximum rainfall seems to concentrate on Indian to Western Pacific oceans, southeast Africa and South America. It is worth to note that velocity potential and convective rainfall are both the strongest over the Western Pacific, which also correlate to largest cloudiness in the TTL.

In July when the NH summer is at its peak, both the velocity potential and rainfall fields exhibit asymmetry with two major convective outflow centers about 10° to 15° of latitude north of the equator over South Asia, and Central America, respectively. The July mean winds are also largely asymmetric about the equator. The NH is dominated by two prominent anti-cyclonic cells over Tibet and Mexico, with oceanic troughs over the Pacific and Atlantic oceans. The rainfall concentrates mostly over Indian monsoon region and south Asia. Central America and northern Africa also have heavy rainfalls. Note there is a local maximum rainfall over the Red Sea which seems to relate to the GW pattern in Figure 4b.

By combining information from the MLS measurements, MWFM, ECMWF and CMAP results, geographic locations of deep-convective activities can be summarized as the following (Figure 11): In NH winter/SH summer, continental deep-convections usually occur in Africa and South America, while deep-convections over water surface most frequently appear in the Western Pacific. The region over Indonesia possibly has combined land and oceanic convections. In NH summer/SH winter, the major deep-convective events occur in regions over the Indian monsoon and Central America monsoon, plus some hurricane (in Gulf Mexico), typhoon (in southeast Asia) and other storm activities over the ocean.

[Insert Figure 11 here]

5. Concluding remarks and future work

Geographical distributions of UTH, TTL cloudiness, and stratospheric GW variances have been analyzed from the UARS MLS observations. These MLS fields are compared to corresponding maps of ECMWF simulated wind divergence and CMAP rainfall rates for different seasons and years. The correlative pattern of the various parameter fields lead to an improved recognition of the causes and effects of tropical/sub-tropical convections in the tropropause and stratosphere worldwide. Combined evidences show that most spatial variations of MLS measured GWs and cloudiness near the tropics are due to the occurrence of regions of strong deep-convection, which result in large spatial and seasonal variations in the air ascending into the TTL.

In December-March, oceanic deep-convection in Western Pacific penetrates the tropopause significantly above the Western Pacific warm pool as indicated by presence of high-altitude clouds near the top of TTL, as well as by the strongest ECMWF velocity potential and CMAP rainfall rate in the region. The deep-convection overshoots of the tropical tropopause result in ~*5%* of ice clouds being lofted to altitude as high as ~68 hPa. High frequency of cloudiness in the TTL is also found over the convective regions of Africa and South America, but only small fraction (≤*1%*) of the cloudiness over these regions reaches altitude above ~100 hPa, especially during the 1992-93 NH winter. The lowest TTL temperature area (or "cold region") is seen to be correlated with the deep-convection and located at slightly downstream side of the deep-convection center. The minimum in water vapor mixing ratio (or "dry region") near the top of TTL is also seen to be shifted slightly north-westward downwind from the deep convection. This might imply that the rapid horizontal and vertical transport of air through cold regions dehydrates air as it ascends. Thus both vertical and horizontal motions are important for understanding the distribution of water vapor.

In July-September, highest frequencies of cloudiness are found over the Indian subcontinent and over Central America. Deep convections related to the Indian Monsoon lift ~*5%* of ice clouds to altitude ~68 hPa. The moistening from the Indian and North American monsoons clearly results two high water vapor mixing ratio regions in the TTL up to ~100 hPa level, suggesting that continental monsoon convections are not actually moistening the TTL. The related TTL low-temperature regions above the Indian monsoon are somewhat south-eastward of the convection area and also seem to following the wind pattern in the region. Minima in water vapor mixing ratio are not aligned well with the convection in this season, which may imply that dehydration in the TTL happens in regions away (i.e. not in the vicinity) from convection.

Strong stratospheric GWs radiated above the convective cloud tops are also measured by MLS. These GWs are correlated well with major convection centers and are shifted poleward by prevailing stratospheric winds, which agrees with the background filtering theory.

The time series of TTL cloudiness frequency for the three SH summertime regional deep-convections show a slightly decreasing trend from 1991-94. But this may not be used as the evidence of a decline in convection events, since the time series of GW variances does not clearly show the same trend. Aside from the possible El Nino and Pinatubo effects, the inter-annual variations of water vapor and cloudiness might be an imprint of the inter-annual cycle of the minimum tropopause temperature on water vapor followed by slow ascent into the stratosphere as suggested by a recent model-measurement comparison study by *Read et al.* [2003].

The above findings from the MLS measurements suggest that both the deep-convection overshoot and the slow-ascent mechanism are important to understand the complicated dehydration processes in the TTL. While making no judgment on these issues here, we would like to point out that deep-convections produce disturbances to an otherwise quiet TTL and thus affect the seasonal temperature and water vapor distributions there. Although, the inter-annual variations in the TTL may indeed indicate a slow ascending trend according to *Read et al.* [2003], both "deep-convection" and "slow-ascent" mechanisms may play a role: deep-convection is important on a shorter time scale (days to seasonal) and slow-ascent on a longer time-scale (inter-annual).

Future observations and analyses of water vapor, ozone, temperature, clouds, and gravity waves data from the new generation EOS MLS and other instruments (e.g. HIRDLS and TES) on board the EOS Aura satellite (to be launched in 2004) will enable the complete convective pattern to be observed with global coverage and greatly improved space-time resolution to capture the dominant scales of organized convection. The EOS MLS is specifically designed to measure water vapor with *0.1-0.2 ppmv* precision throughout the TTL at *2.7 km* vertical resolution. The cirrus ice measurement from EOS MLS may provide details of whether the ice masses lofted into the TTL are from the deep-convection. The EOS MLS upper-tropospheric ozone measurements could also provide useful information. For example, low ozone near the TTL may indicate air that has been recently being transported from the boundary layer via deep-convection. Thus a positive coincidence between regions of low water vapor and low ozone could support a convective dehydration hypothesis (*A. Dessler*, personal communication). These future endeavors will provide us with an integrated picture and better information of the dynamic and thermodynamic conditions in the TTL, and the issues related to long-term stratospheric water-vapor variations.

Acknowledgements

Dr. Klemens Hocke's typical enthusiasm brought this collaborated research together, and he sent his support to us from a hospital bed in Germany just before the submission of this manuscript. We continue contact with him. Many initial ideas of this paper came from the discussions with the scientists attending the October 2002 Houston COSPAR conference. Dr. Joe W. Waters prepared the COSPAR presentation paper and fellow colleagues in the MLS science team provide encouragements and helpful suggestions. We thank J. R. Holton, J. C. McConnell, A. E. Dessler, P. H. Haynes, and M. J. Schwartz who provided valuable comments to improve the manuscript. This work was supported by the Jet Propulsion Laboratory, California Institute of Technology, under contract with the National Aeronautics and Space Administration. The authors also acknowledge the supports by Department of Meteorology, University of Hawaii; Geophysical Fluid Dynamics Laboratory at Kyushu University of Japan; the Naval Research Laboratory of Washington DC; and the Computational Physics, Inc., Virginia.

References

Alexander, M. J., J. R. Holton and D. R. Durran, The gravity wave response above deep convection in a squall line simulation, *J. Atmos. Sci.*, 52, 2212-2226, 1995.

Alexander, M. J., J. H. Beres, and L. Pfister, Tropical stratospheric gravity wave activity and relationship to clouds, *J. Geophys. Res.*, 105, 22,299-22,309, 2000.

Boehm, M. T., and J. Verlinde, Stratospheric influence on upper tropospheric tropical cirrus, *Geophys. Res. Lett.*, 27, 3209-3212, 2000.

Booker, J. R. and F. P. Bretherton, The critical layer for internal gravity waves in a shear flow, J. *Fluid. Mech.*, 27, 513-539, 1967.

Brewer, A. M., Evidence for a world circulation provided by the measurements of helium and water vapor distribution in the stratosphere, *Quart. J. Roy. Meteorol. Soc.*, 75, 351-363, 1949.

Clark, H. L., A. Billingham, R. S. Harwood, and H. C. Pumphrey, Water vapor in the tropical lower stratosphere during the driest phase of the atmospheric "tape recorder", *J. Geophys. Res.*, 106, 22,695-22,705, 2001.

Dessler, A. E., and H. Kim, Determination of the amount of water vapor entering the stratosphere based on Halogen Occulation Experiment (HALOE) data, *J. Geophys. Res.*, 104, 30,605-30607, 1999.

Dessler, A. E., and S. C. Sherwood, Simulations of tropical upper tropospheric humidity, *J. Geophys. Res.*, 105, 20155-20163, 2000.

Eckermann, S. D., J. H. Jiang, J. Ma, and D. L.Wu, A model simulation of stratospheric mountain waves in the southern hemisphere winter, manuscripts in preparation, 2003.

Fleming, E. L., S. Chandra, J. J. Barnett and M. Corney, Zonal mean temperature, pressure, zonal wind, and geopotential height as functions of latitude, *Adv. Space Res.*, 10(12), 11-59, 1990.

Forster, P. M. D. F., and K. P. Shine, Stratospheric water vapor changes as a possible contributor to observed stratospheric cooling, *Geophys. Res. Lett.*, 26, 3309-3312, 1999.

Fovell, R., D. Durran, and J. R. Holton, Numerical simulations of convectively generated stratospheric gravity waves, *J. Atmos. Sci.*, 49, 1427-1442, 1992.

Fritts, D. C., and T. E. VanZandt, Spectral estimates of gravity wave energy and momentum fluxes, I, energy dissipation, acceleration, and constraints, *J. Atmos. Sci., 50*, 3685–3694, 1993.

Fu, X., and B. Wang, A coupled modeling study of the seasonal cycle of the Pacific cold tongue Part I: simulation and sensitivity experiments, *J. Climate*, 765-779, 2001.

Geller, M. A., H. Tanaka and D. C. Fritts, Production of turbulence in the vicinity of critical levels for internal gravity waves, *J. Atmos. Sci.*, 32, 2125-2135, 1975.

Gettelman, A., A. R. Douglass, and J. R. Holton, Simulations of water vapour in the upper troposphere and lower stratosphere, *J. Geophys. Res.*, 105, 9003-9023, 2000.

Goya, K., Non-hydrostatic and compressible 2-d model simulations of internal gravity waves, *Doctoral thesis*, Kyushu University, 1998.

Goya, K. and S. Miyahara, A non-hydrostatic and compressible 2-D model simulation of Internal Gravity Waves generated by convection, *Earth Planets Space*, 51, 485-498, 1998.

Goya, K. and S. Miyahara, Non-hydrostatic nonlinear 2-D model simulations of internal gravity waves in realistic zonal winds, *Advances in Space Research*, 24, 1523-1526. 1999.

Hall, T. J., and T. H. Vonder Harr, The diurnal cycle of west Pacific deep convection and its relation to the spatial and temporal variations of tropical MCSs, *J. Atmos. Sci.,* 56, 3401-3415, 1999.

Highwood, E. J., and B., J., Hoskins, The tropical tropopause, *Quart. J. Roy. Meteorol. Soc.,* 124, 1579-1604, 1998.

Holton, J. R., An introduction to dynamic meteorology (3rd Edition), *Academic Press*, 1992.

Holton, J. R., and A. Gettelman, Horizontal transport and the dehydration of the stratosphere, *Geophys. Res. Lett*., 28, 2799-2802, 2001.

Holton, J. R., M. J. Alexander, and M. T. Boehm, Evidence for short vertical wavelength Kelvin waves in the DOE-ARM Nauru99 radiosonde data*, J. Geophys. Res*., 106, 20,125-20129, 2001.

Holton, J. R. and M. J. Alexander, Gravity waves in the mesosphere generated by tropospheric convection, *Tellus*, 51A-B, 45-58, 1999.

Hendon, H. H., and K. Woodberry, The diurnal cycle of tropical convection, *J. Geophys. Res.*, 98, 16,623-16,637, 1993.

Jensen, E. J., O. B. Toon, H. B. Selkirk, J. D. Spinhime, and M. R. Schoberl, On the formation and persistence of subvisible cirrus clouds near the tropical tropopause, *J. Geophys. Res*., 101(D16), 21,361-21,375, 1996.

Jiang, J. H., and D. L. Wu, UARS MLS observation of gravity waves associated with the Arctic winter stratospheric vortex, *Geophys. Res. Lett*., 28, 527-530, 2001.

Jiang, J. H., D. L. Wu, S.D. Eckermann, Upper Atmosphere Research Satellite (UARS) MLS observation of mountain waves over the Andes, *J. Geophys. Res*. 107, D22, 10.1029 /2002JD002091, 2002.

Jiang, J. H., S. D. Eckermann, D.L.Wu, and J. Ma, Mountain waves in the middle atmosphere: microwave limb sounder observations and analyses, *Adv. Space. Res*., in press, 2003a.

Jiang, J. H., S. D. Eckermann, D. L. Wu, and J. Ma, A search for mountain waves in MLS stratospheric limb radiances from the winter northern hemisphere: Data analysis and global mountain wave modeling, *J. Geophys. Res.*, submitted, 2003b.

Johnson, R. H., and D. C. Kriete, Thermodynamic and circulation characteristics of winter monsoon tropical mesoscale convection, *Mon. Weather Rev*., 110, 1898-1911, 1982.

Johnston, H. S., and S. Solomon, Thunderstorms as possible micrometeorological sink for stratospheric water, *J. Geophys. Res*., 84, 3155-3158, 1979.

Karoly, D. J., G. L. Roff, and M. J. Reeder, Gravity wave activity associated with tropical convection detected in TOGA COARE sounding data, *Geophys. Res. Lett*., 23, 261-264, 1996.

Kirk-Davidoff, D. B., E. J. Hintsa, J. G. Anderson, and D. W. Keith, The effect of climate change on ozone depletion through changes in stratospheric water vapour, *Nature*, 402, 399-401, 1999.

Koch, S. E., and L. M. Siedlarz, Mesoscale gravity waves and their environment in the central United States during STORM-FEST, Mon. Weather Rev., 127, 2854-2879, 1999.

Lane, T. P., M. J. Reeder, and T. L. Clark, Numerical modeling of gravity wave generation by deep tropical convection, *J.Atmos. Sci*., 58, 1249-1274, 2001

Liu, G., J. A. Curry, and R. S.. Sheu, Classification of clouds over the western equatorial Pacific ocean using combined infrared and microwave satellite data, *J. Geophys. Res*., 100, 13,811-13,826, 1995.

Liu, X., and J. Penner, Effect of Mount Pinatubo H_2SO_4/H_2O aerosol on ice nucleation in the upper troposphere using a global chemistry and transport model, *J. Geophys. Res*., 107(D12), 10.1029/2001JD000455, 2002.

Livesey, N. J., and D. L. Wu, Eos MLS retrieval processes algorithm theoretical basis, JPL Document *D-16159, EOS MLS DRL 601 (part 3), ATBD-MLS-03*, 1999.

Livesey, N.J., W.G. Read, L. Froidevaux, J.W. Waters, H.C. Pumphrey, D.L. Wu, M.L. Santee, Z. Shippony, R.F. Jarnot, "The UARS Microwave Limb Sounder version 5 dataset: Theory, characterization and validation," *J. Geophys. Res., in press*, 2003.

Lohmann, U., B. Kaercher and C. Timmreck, Impact of the Mt. Pinatubo Eruption on cirrus clouds formed by homogeneous freezing in the ECHAM GCM, *J. Geophys. Res.*, 108, in press, 2003.

Mapes, B., and R. Houze, Cloud clusters and superclusters over the oceanic warm pool, *Mon. Wea. Res*., 121, 1398-1415, 1993.

Massie, S., P. Lowe, X. Tie, M. Hervig, G. Thomas, and J. Russell III, Effect of the 1997 El Nino on the distribution of upper tropospheric cirrus, *J. Geophys. Res*., 105(D18), 22,725-22,741, 2000.

McLandress, C., M. J. Alexander, D. L. Wu, Microwave Limb Sounder observations of gravity waves in the stratosphere: A climatology and interpretation, *J. Geophys. Res*., 105, 11947-11967, 2000.

Mote, P. W., K. H. Rosenlof, M. E. McIntyre, E. S. Carr, J. R. Holton, J. S. Kinnersley, H. C. Pumphrey, J. M. Russell III, J. W. Waters, and J. C. Gille, An atmospheric tape recorder: The imprint of tropical tropopause temperatures on stratospheric water vapor, *J. Geophys. Res*., 101, 3989-4006, 1996.

Murakami, T., and B. Wang, Annual cycle of Equatorial east-west circulation over the India Pacific oceans, *J. Climate*, Vol 6, 932-952, 1993.

Newell, R. E., and S. Gould-Stewart, A stratospheric fountain? J. Atmos. Sci., 38, 2789-2796, 1981.

Piani, C., D. Durran, M. J. Alexander and J. R. Holton, A numerical study of three-dimensional gravity waves triggered by deep tropical convection and their role in the dynamics of the QBO, *J. Atmos. Sci*., 57, 3689-3702, 2000

Preusse, P., G. Eidmann, S. D. Eckermann, B. Schaeler, R. Spang, and D. Offermann, Indications of convectively generated gravity waves in CRISTA temperatures, *Adv. Space. Res*., 27(10), 1653-1658, 2001.

Randel, W. J., F. Wu, and D. Gaffen, Low frequency variations of the tropical tropopause from NCEP reanalyses, *J. Geophys. Res*., 105, 15,509-15,523, 2000.

Randel, W. J., F. Wu, A. Gettelman, J. M. R. III, J. M. Zawodny, and S. J. Oltmans, seasonal variation of water vapor in the lower stratosphere observed in Halogen Occultation Experiment data, *J. Geophys. Res*., 106, 14,313-14,325, 2001.

Read, W. G, J. W. Waters, D. L. Wu, E. M. Stone, Z. Shippony, A. C. Smedley, C. C. Smallcomb, S. Oltmans, D. Kley, H. G. J. Smit, J. L. Mergenthaler, M. K. Karki, "UARS Microwave Limb Sounder Upper Tropospheric Humidity Measurement: Method and Validation," *J. Geophys. Res*. 106, 32,207-32,258, 2001.

Read, W. G., D. L. Wu, J. W. Waters, and H. C. Pumphrey, H_2O in the tropical tropopause layer measured by UARS MLS, submitted to *J. Geophys. Res*., 2003

Roach, R., and V. Ramanathan, Scale dependence of monsoonal convective systems over the Indian ocean, *J. Climate*, 13, 1286-1298, 2000.

Salby, M. L., Fundamentals of atmospheric physics, 440p, *Academic Press*, 1996.

Sherwood, S. C., A "stratospheric drain" over the martitime continent, *Geophys. Res. Lett.*, 27, 677-680, 2000.

Sherwood, S. C., and A. E. Dessler, On the control of stratospheric humidity, *Geophys. Res. Lett.*, 27, 2513-2516, 2000.

Sherwood, S., C., and A. E. Dessler, A model for transport across the tropical tropopause, *J. Atmos. Sci.,* 58, 765-779, 2001.

Soden, B., The diurnal cycle of convection, clouds, and water vapor in the tropical upper troposphere, *Geophys. Res. Lett*., 27, 2173-2176, 2000.

Teitelbaum, H., M. Moustaoui, C. Basdevant, and J. R. Holton, An alternative mechanism explaining the hygropause formation in tropical region, *Geophys. Res. Lett.,* 27, 221-224, 2000.

Tsuda, T., Y. Murayama, H. Wiryosumarto, S. W. B. Harijino, and S. Kato, Radiosonde observations of equatorial atmospheric dynamics over Indonesia 1. Equatorial waves and diurnal tides, *J. Geophys. Res*., 99, 10,491-10,505, 1994a.

Tsuda, T., Y. Murayama, H. Wiryosumarto, S. W. B. Harijino, and S. Kato, Radiosonde observations of equatorial atmospheric dynamics over Indonesia 2. Characteristics of gravity waves, *J. Geophys. Res*., 99, 10,507-10,516, 1994b.

Tsuda, T., M. Nishida, C. Rocken, and R. H. Ware, A global morphology of gravity wave activity in the stratosphere revealed by the GPS occultation data (GPS/MET), *J. Geophys. Res.*, 105, 7257-7273, 2000.

Vadas, S. L. et al, Mechanism for the generation of secondary waves in wave breaking regions, *J. Atmos. Sci.*, in press, 2003. (private communication in 2002).

Waters, J.W., W.G. Read, L. Froidevaux, R.F. Jarnot, R.E. Cofield, D.A. Flower, G.K. Lau, H.M. Pickett, M.L. Santee, D.L. Wu, M.A. Boyles, J.R. Burke, R.R. Lay, M.S. Loo, N.J. Livesey, T.A. Lungu, G.L. Manney, L.L. Nakamura, V.S. Perun, B.P. Ridenoure, Z. Shippony, P.H. Siegel, R.P. Thurstans, R.S. Harwood, H.C. Pumphrey, M.J. Filipiak, The UARS and EOS Microwave Limb Sounder Experiments, *J. Atmos. Sci.*, 56, 194-218, 1999.

Wang, B., On the annual cycle in the tropical eastern central Pacific, *J. Climate*, Vol 7, 1926-1942, 1994.

Wang, B., Climate regimes of tropical convection and rainfall, *J. Climate*, Vol 7, 1109-1118, 1994.

Wang, B., and Y. Wang, Dynamics of the ITCZ-Equatorial cold tongue complex and causes of the latitudinal climate asymmetry, *J. Climate*, Vol 12, 1830-1847, 1998.

Wu, D. L., and J. H. Jiang, MLS observation of atmospheric gravity waves over Antarctica, *J. Geophys. Res.*, 107, No. D24, 4773, 10.1029/2002JD002390, 2002a.

Wu, D. L., and J. H. Jiang, EOS MLS Algorithm Theoretical Basis for Cloud Measurements, JPL Document (draft) *D-19299, EOS MLS DRL 601 (part x), ATBD-MLS-0x*, 2002b.

Wu, D. L., J. H. Jiang, W. G. Read, and J. W. Waters, A cloudy-sky radiative transfer model for microwave limb sounding, manuscript in preparation, 2003.

Wu, D. L., and J. W. Waters, Satellite observations of atmospheric variances: A possible indication of gravity waves, *Geophys. Res. Lett.*, 23, 3631-3634, 1996a.

Wu, D. L., and J. W. Waters, Gravity-wave-scale temperature fluctuations seen by the UARS MLS, *Geophys. Res. Lett.*, 23, 3289-3292, 1996b.

Zhou, X., M. A. Geller, and M. Zhang, The cooling trend of the tropical cold point tropopause temperatures and its implications, *J. Geophys. Res.*, 106, 1511-1521, 2001.

Jonathan H. Jiang, Jet Propulsion Laboratory, California Institute of Technology, Mail-Stop 183-701, 4800 Oak Grove Drive, Pasadena, California 91109-8099, U.S.A. E-mails:jonathan@mls.jpl.nasa.gov.

December-March, 1991-92

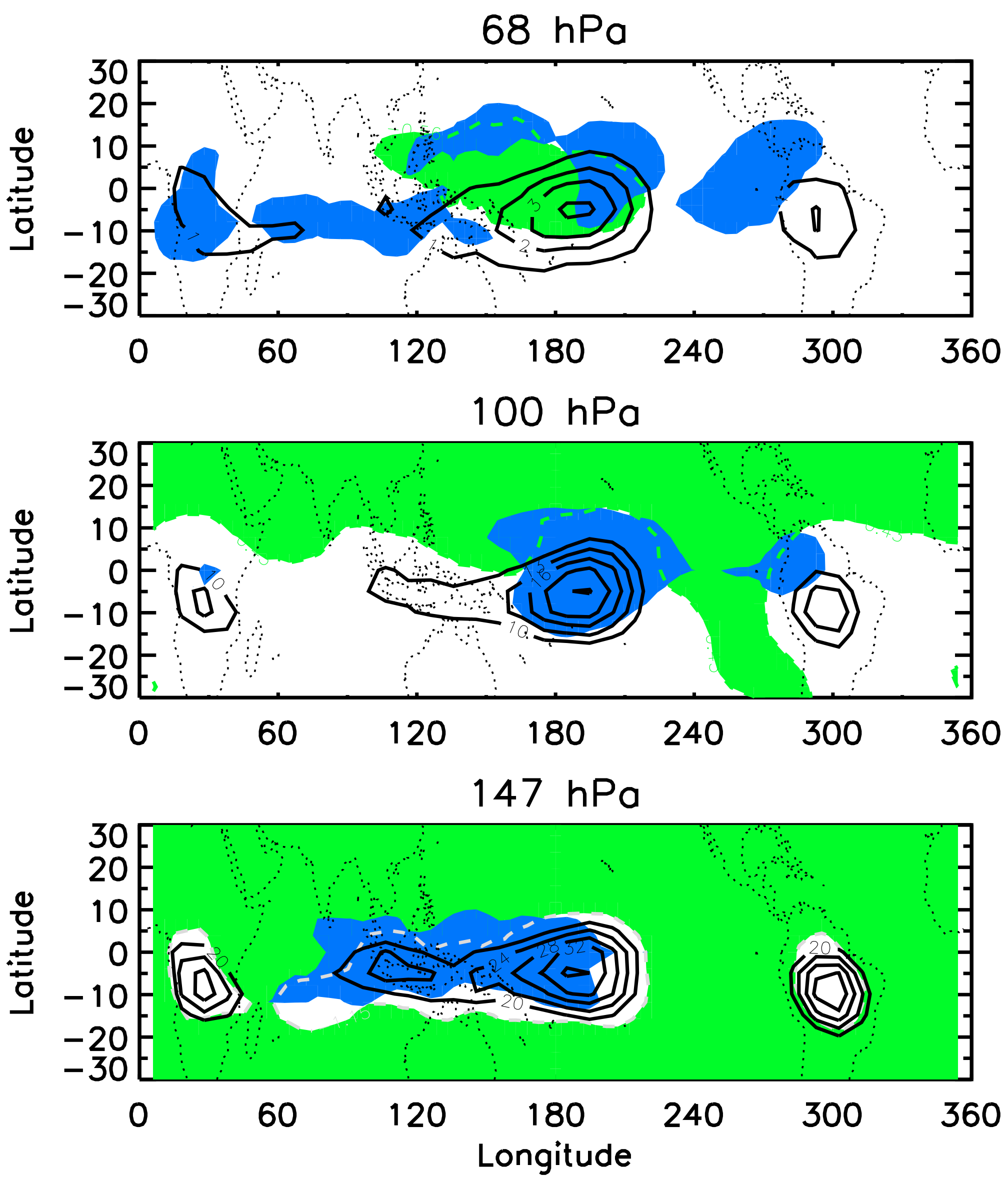

Tropical Wind Profiles (Dec-Mar, 91-92)

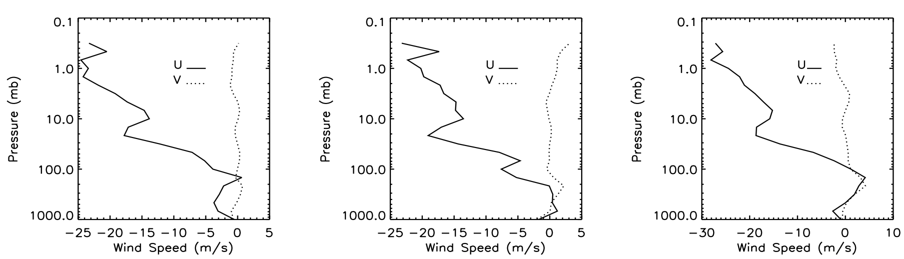

Southern Africa
Lat: [4°N-12°S]
Lon: [5°-50°]

Western Pacific
Lat: [8°N-12°S]
Lon:[115°-220°]

South America
Lat: [4°N-12°S]
Lon:[280°-310°]

Figure 1a

Figure 1a: Black-line contours are the MLS measured cloudiness averaged for December-March 1991-92 (the contour-labels are values in *%*). At *147 hPa*, *100 hPa* and *68 hPa* altitudes, only contours with cloudiness frequencies $\geq 20\%$, $\geq 10\%$ and $\geq 1\%$ are shown, respectively. The green-colored areas are regions with the lowest value of v7.02 water vapor mixing ratio (≤ 14.03 *ppmv* for *147 hPa*, ≤ 2.67 *ppmv* for *100 hPa*, and ≤ 3.60 *ppmv* for *68 hPa*). The blue-colors represent regions with the lowest temperature ($\leq -68.0\,^\circ C$ at *147 hPa*, $\leq -79.3\,^\circ C$ at *100 hPa,* and $\leq -74.8\,^\circ C$ at *68 hPa*). The temperatures are computed from the UKMO (United Kingdom Meteorological Office) assimilated temperature data, interpolated onto UARS orbits and averaged according to MLS measurement days. The lowest-water-vapor regions covered behind the lowest-temperature plots are indicated by the dashed-green-lines. The data are averaged on (10°×5°) longitude-latitude grids and a 3-point smooth is applied to all the fields. Also plotted in the bottom panel is the UKMO mean wind (U,V) profiles for the three major convection centers.

December-March, 1992-93

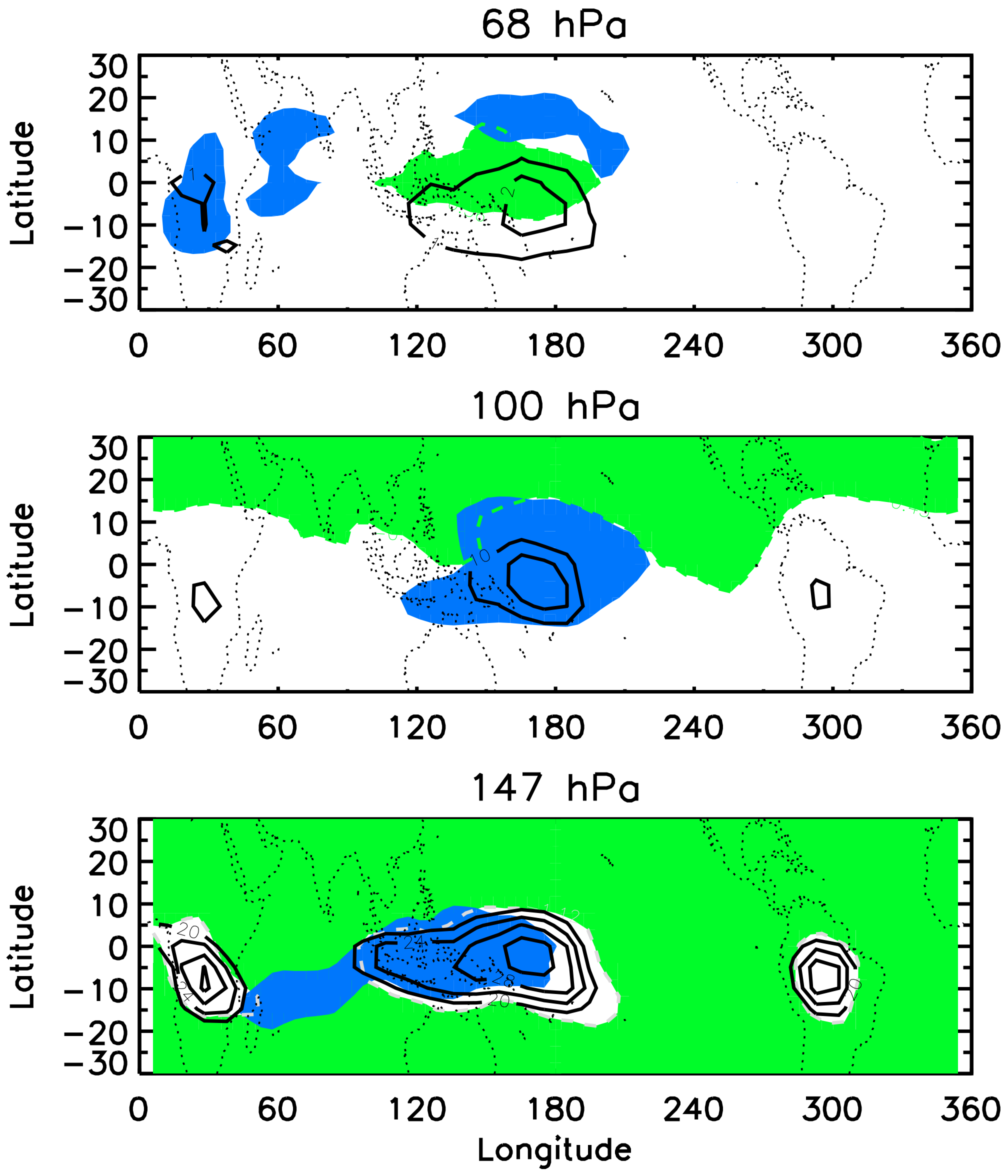

Tropical Wind Profiles (Dec-Mar, 91-92)

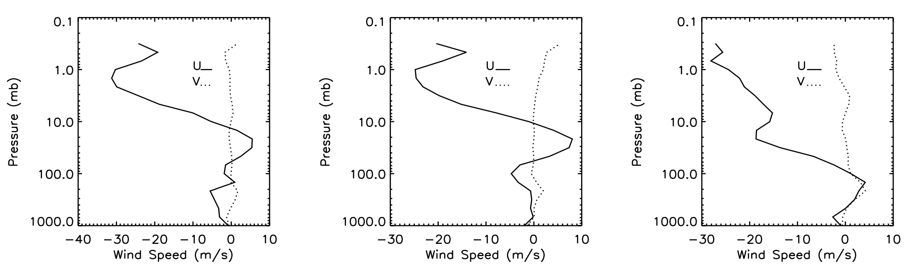

Southern Africa
Lat: [4°N-12°S]
Lon: [5°-50°]

Western Pacific
Lat: [8°N-12°S]
Lon:[115°-220°]

South America
Lat: [4°N-12°S]
Lon:[280°-310°]

Figure 1b

Figure 1b: Cloudiness contours and contour-labels are defined the same as in Figure 1a but for December-March of 1992-93. The green-colored areas are regions with the lowest value of water vapor mixing ratio ($\leq$ *13.18 ppmv* for *147 hPa*, $\leq$ *2.67 ppmv* for *100 hPa*, and $\leq$ *3.60 ppmv* for *68 hPa*). The blue-colors represent regions with the lowest UKMO temperature ($\leq -68.7\,^{\circ}C$ at *147 hPa*, $\leq -79.3\,^{\circ}C$ at *100 hPa,* and $\leq -74.3\,^{\circ}C$ at *68 hPa*). Note the minimum values of water vapor and temperature used to draw the region boundary here is slightly different from that of Figure 1a. Note that our focus is the *distribution* of these minimum water vapor and temperature regions, not their actual values. The UKMO mean wind profiles are also shown for the major convection centers.

June-September, 1992

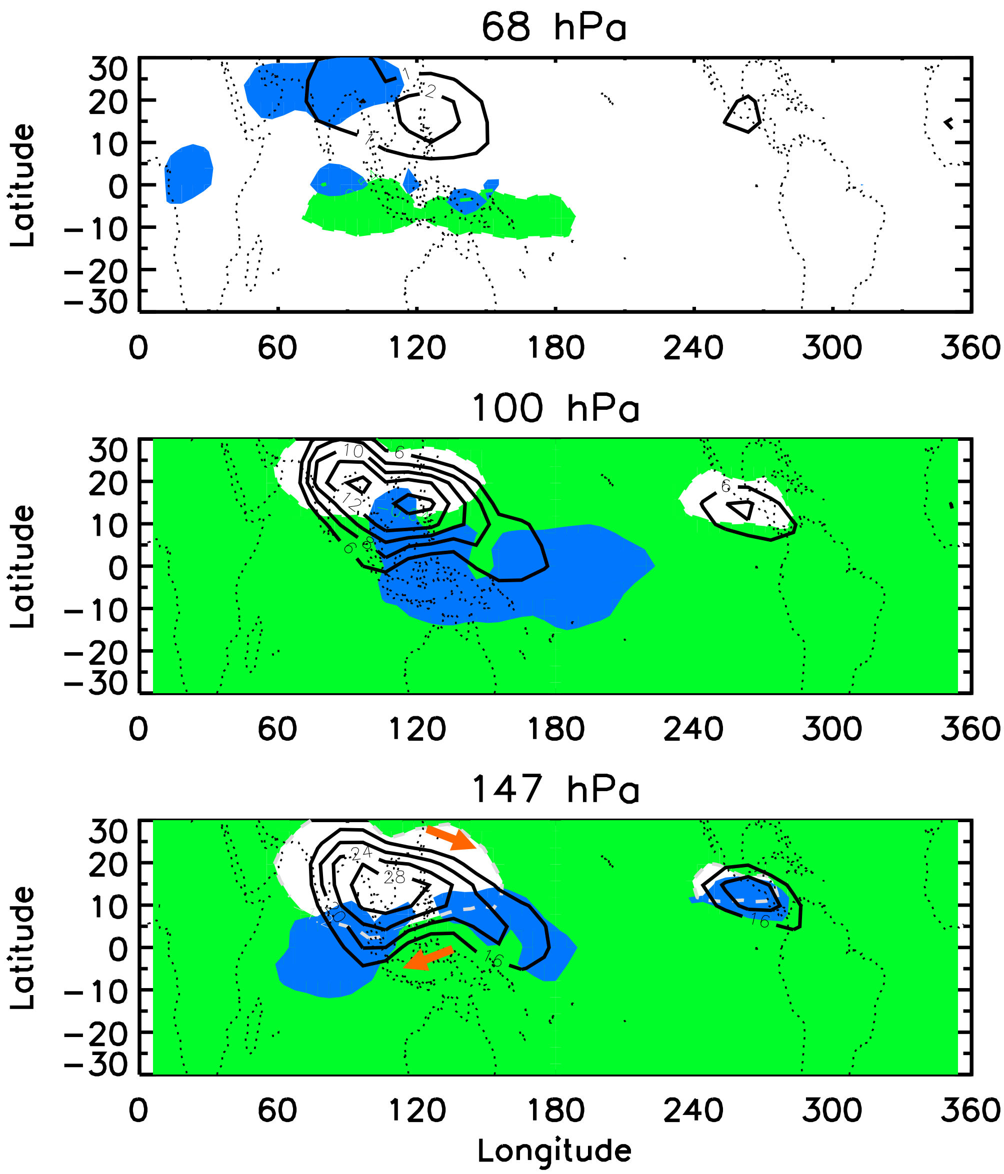

Tropical Wind Profiles (Jun-Sep, 92)

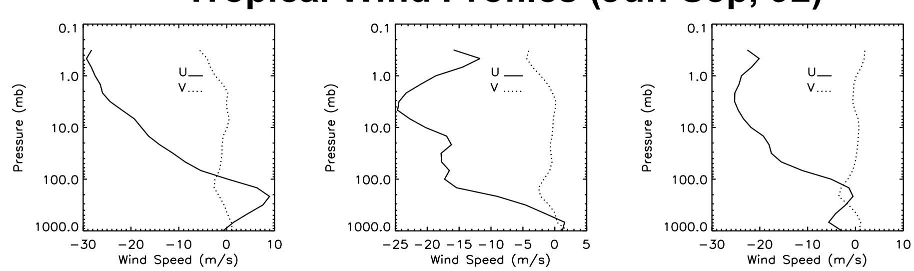

Tibet	**South Asia**	**American Monsoon**
Lat: [24°N-32°N]	Lat: [8°N-20°N]	Lat: [8°N-24°N]
Lon: [80°-150°]	Lon: [80°-150°]	Lon:[260°-300°]

Indian Monsoon

Figure 1c

Figure 1c: Black-line contours are the MLS measured cloudiness averaged for June-September of 1992 (the contour-labels are values in *%*). At *147 hPa*, *100 hPa* and *68 hPa* altitudes, only contours with cloudiness frequencies *16%*, *6%* and *1%* are shown, respectively. The green-colored areas are the regions with the lowest value of water vapor mixing ratio ($\leq$ *16.03 ppmv* for *147 hPa*, $\leq$ *4.37 ppmv* for *100 hPa*, and $\leq$ *3.47 ppmv* for *68 hPa*). In other words, it's easier to see here that the white-colored areas un-colored by the green-colors are the regions with high value of water vapor mixing ratios. The blue-colors represent regions with the lowest UKMO temperature ($\leq -68.4\,^{\circ}C$ at *147 hPa,* $\leq -75.8\,^{\circ}C$ at *100 hPa,* and $\leq -69.7\,^{\circ}C$ at *68 hPa*). UKMO mean wind profiles are also shown for the two major monsoon regions.

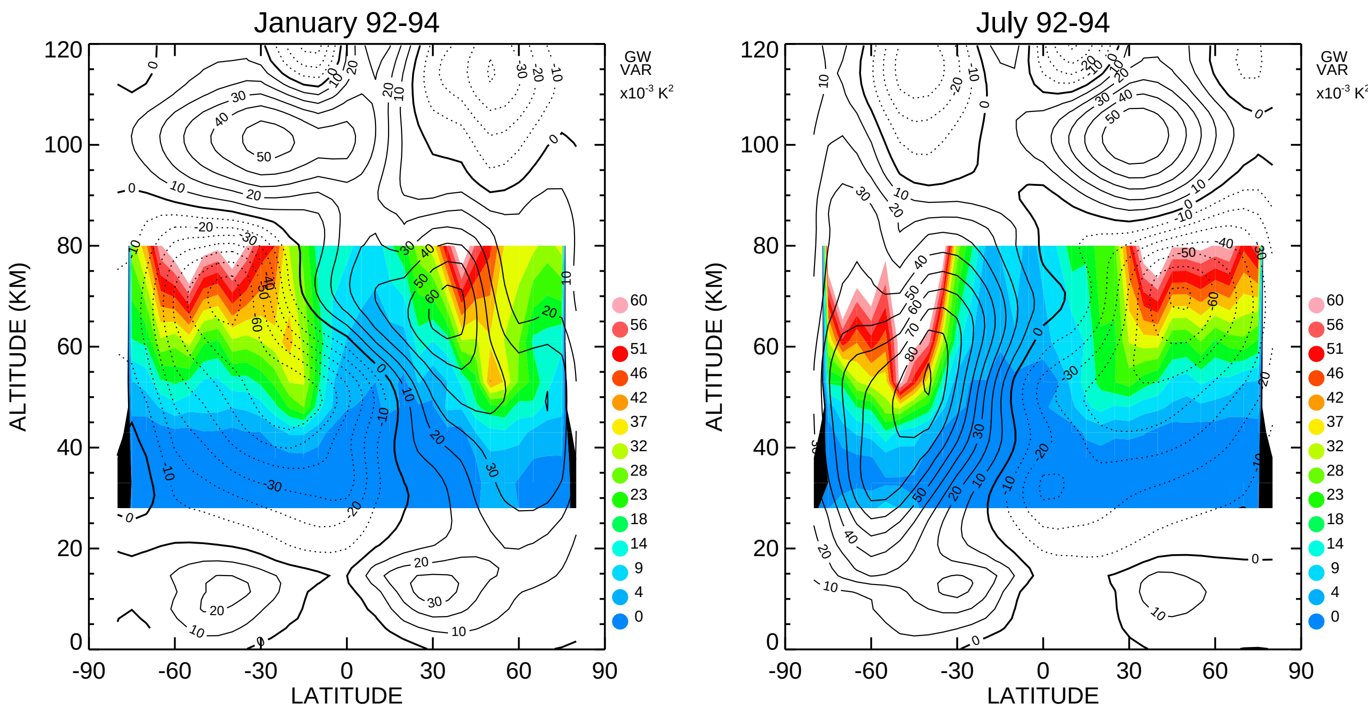

Figure 2: This diagram shows MLS zonal mean GW variances (color-filled contours) for January 1992-94 (left) and July 1992-94 (right), in comparisons with the CIRA (COSPAR International Reference Atmosphere) zonal wind climatology [*Fleming, et al.*, 1990]. The black solid-lines show easterlies, and dotted-lines are westerly winds. The instrument noises have been removed from the GW variances. Note in summer hemispheres, the GW variances shift poleward when propagating upward into the stratosphere.

Figure 2

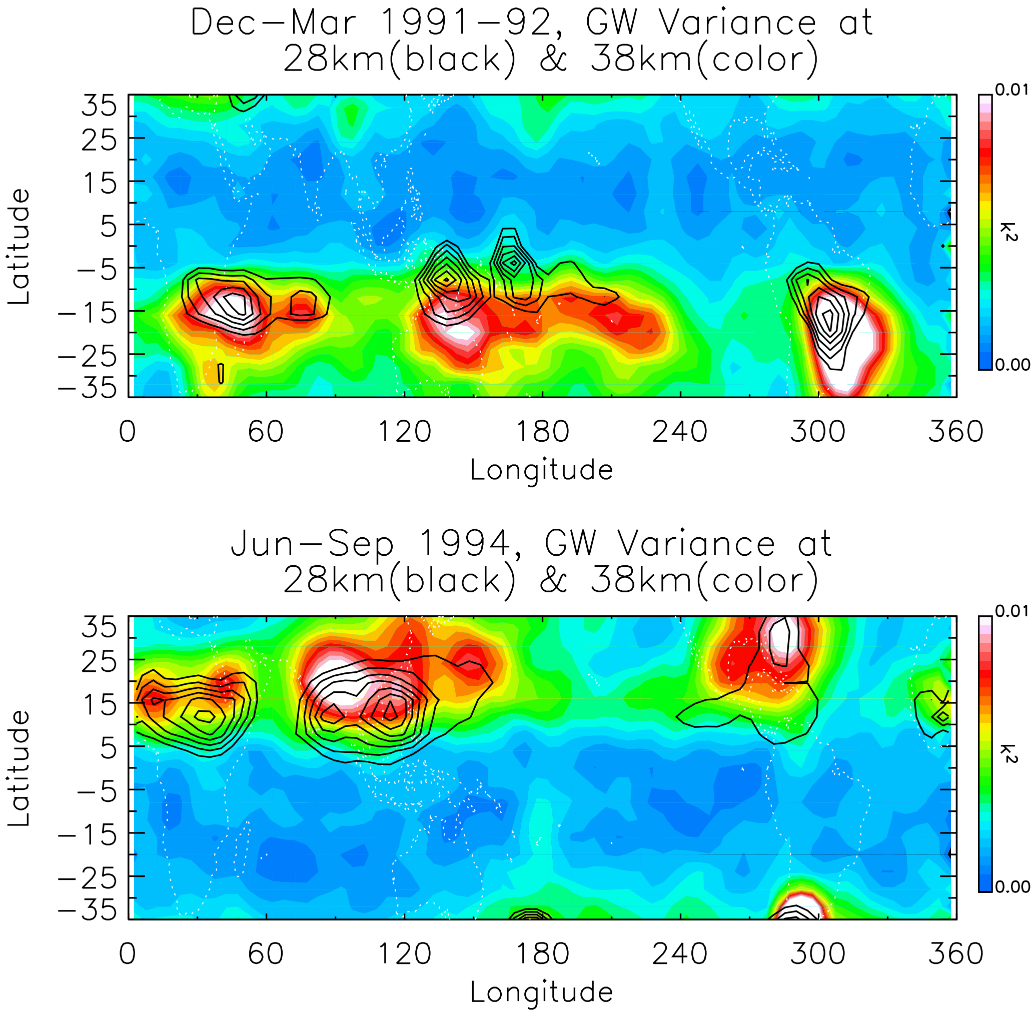

Figure 3: Color-filled maps are the MLS limb-scan GW variances at *38 km* altitudes averaged for December-March of 1991-92 (top), and July-September 1994 (Bottom), respectively, from UARS MLS north-looking ascending and south-looking descend orbits. The black contours are the same GW variances but computed for lower altitudes at *28 km* (contour level-range are 0.002-0.005 k^2). Instrument noises for both altitudes have been removed. Note the centers of the GW activities at *28 km* are closer to convection sources near the equator than the GWs at *38 km*. The data are averaged on (10°×4°) longitude-latitude grids and a 3-point running window mean is applied to smooth all the fields.

Figure 3

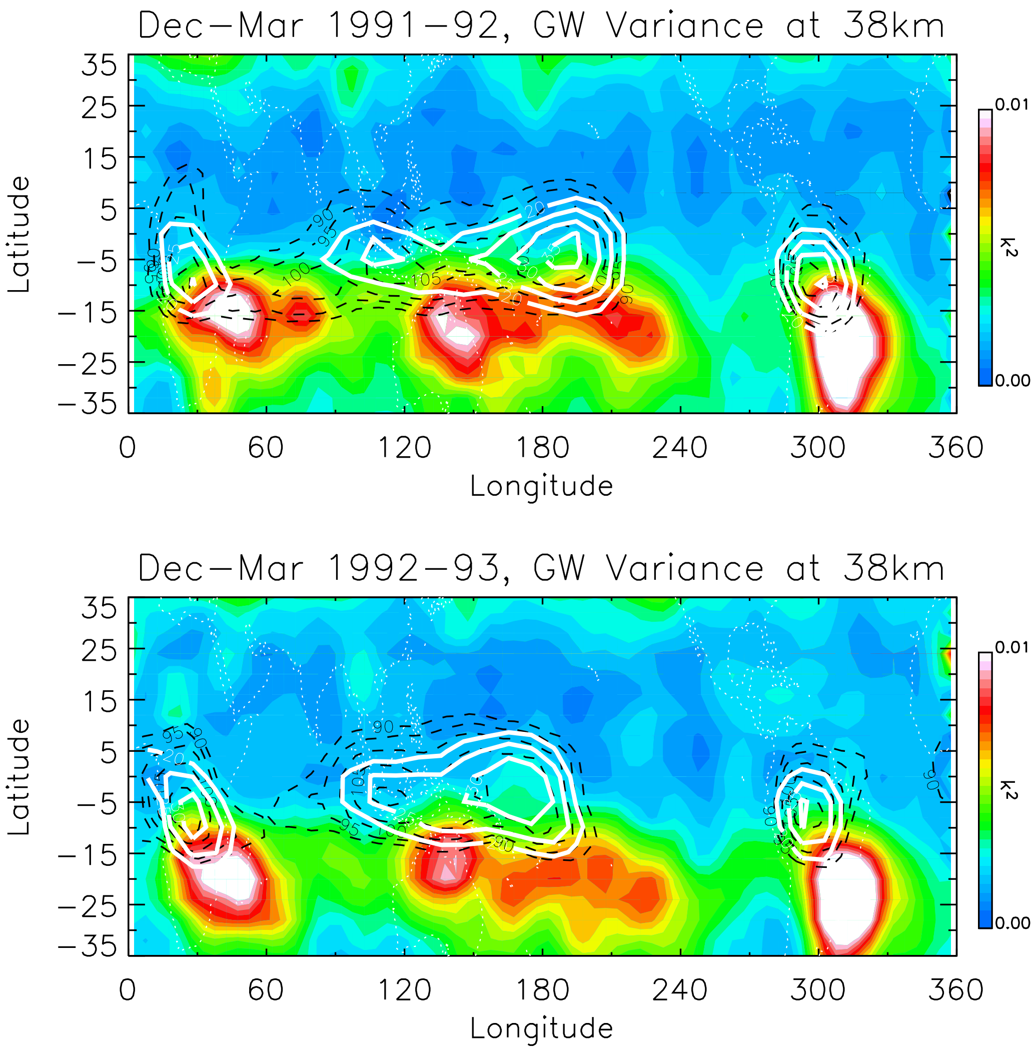

Figure 4a: The color-filled maps are the mean MLS limb-scan GW variances at *38 km* for December-March of 1991-92 (top), 1992-93 (bottom), respectively, and averaged using data taken from UARS MLS north-looking ascending and south-looking descend orbits. The instrument noise has been removed. The white contours are the MLS measured cloudiness (*%*) at *147 hPa*. Only contours with cloudiness frequency ≥ *20%* are shown. Black contours are relative humidity (*RHi*), also at *147 hPa*. Only contours with *RHi ≥ 90%* are shown. We use the V4.9 data set for *RHi* in Figure 4 because it has longer time coverage permitting better comparison with the GW variance maps. Our analyses (not shown here) found the difference between V4.9 and V701 *RHi* is less than *1%* within available MLS measurement days.

Figure 4a

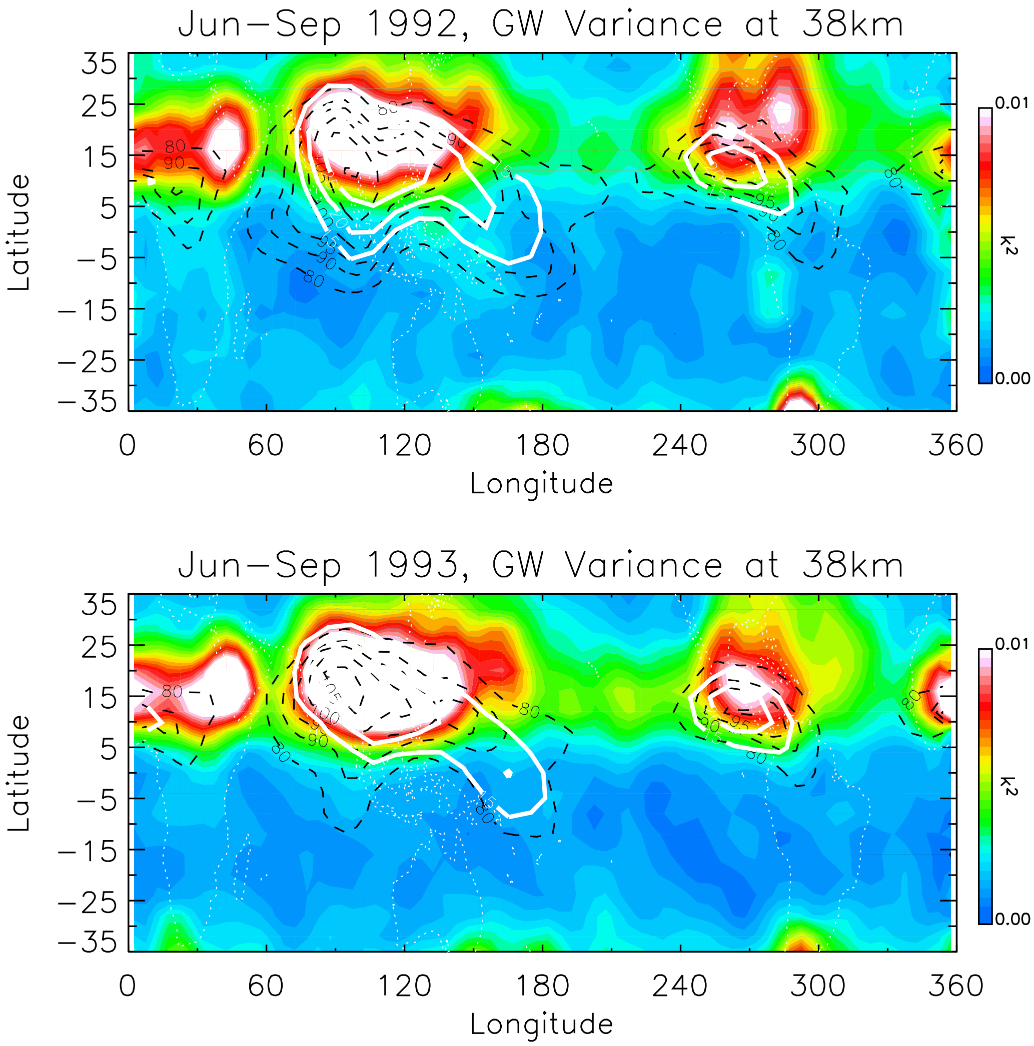

Figure 4b: Same as in Figure 2a except the fields are averaged for July-September of 1992 (top), 1993 (bottom), respectively. Only contours with cloudiness frequency ≥ *15%* are shown. Black contours are relative humidity (*RHi*), also at *147 hPa*. Only contours with RHi ≥ *80%* are shown.

Figure 4b

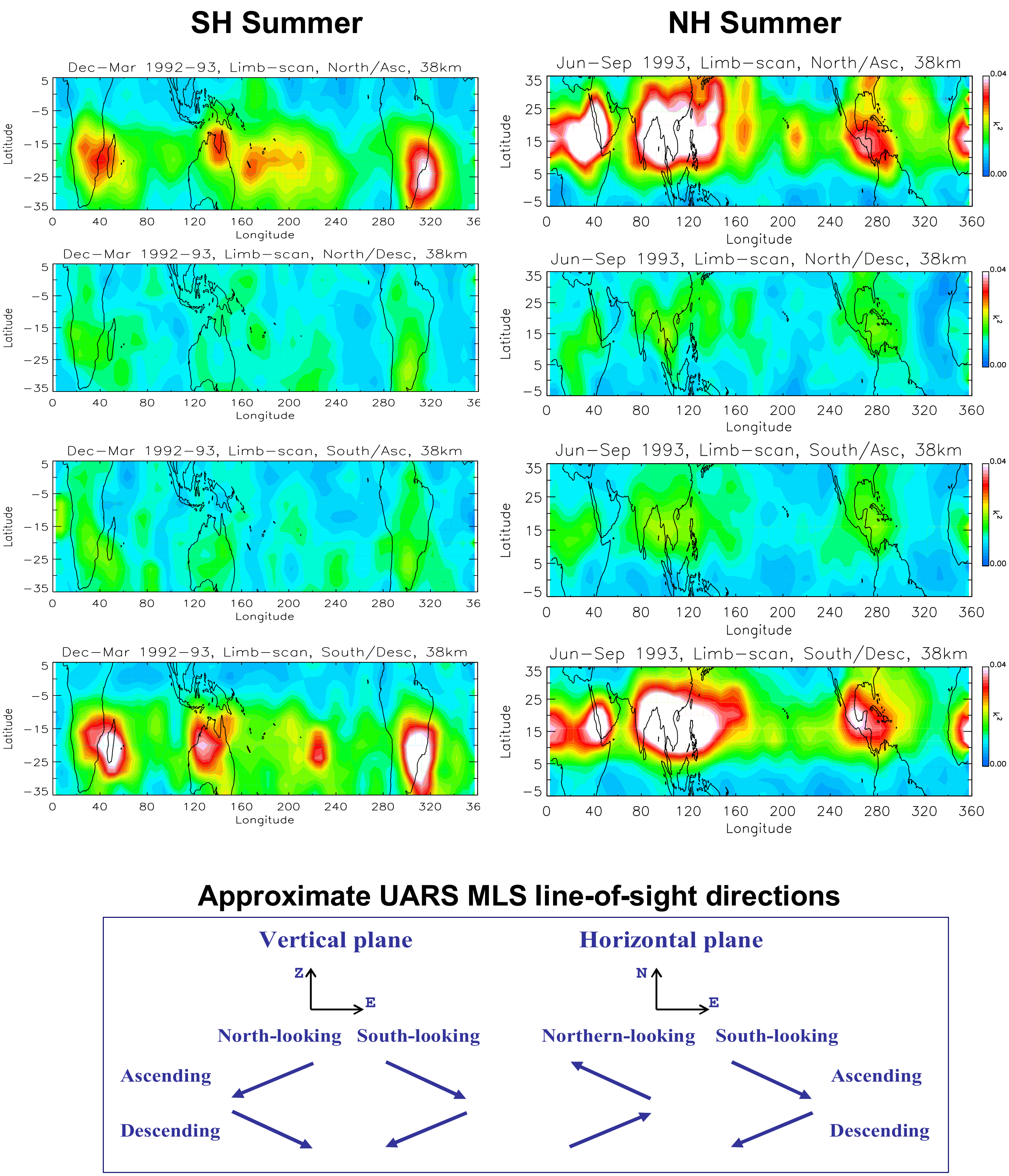

SH Summer
NH Summer
Dec−Mar 1992−93, Limb−scan, North/Asc, 38km
Dec−Mar 1992−93, Limb−scan, North/Desc, 38km
Dec−Mar 1992−93, Limb−scan, South/Asc, 38km
Dec−Mar 1992−93, Limb−scan, South/Desc, 38km
Jun−Sep 1993, Limb−scan, North/Asc, 38km
Jun−Sep 1993, Limb−scan, North/Desc, 38km
Jun−Sep 1993, Limb−scan, South/Asc, 38km
Jun−Sep 1993, Limb−scan, South/Desc, 38km
Latitude
Longitude
0.04
0.00
Approximate UARS MLS line-of-sight directions
Vertical plane
Horizontal plane
Z
E
N
E
North-looking
South-looking
Northern-looking
South-looking
Ascending
Descending
Ascending
Descending

Figure 5

Figure 5: Examples of MLS GW variances measured from different observational modes. Left-column: December-March of 1992-93; Right-column: July-September of 1993. First-row: data from north-looking ascending orbits; Second-row: north-looking descending orbits; Third-row: south-looking ascending orbits; Fourth-row: south-looking descending orbits. Note the convection generated GWs produce stronger signals detectable by MLS on north-looking ascending (first-row) and south-looking descending orbits (fourth-row), when the MLS LOS is looking mostly westward and is scanning the atmosphere from top to surface. The approximate MLS directions are shown at the bottom panel.

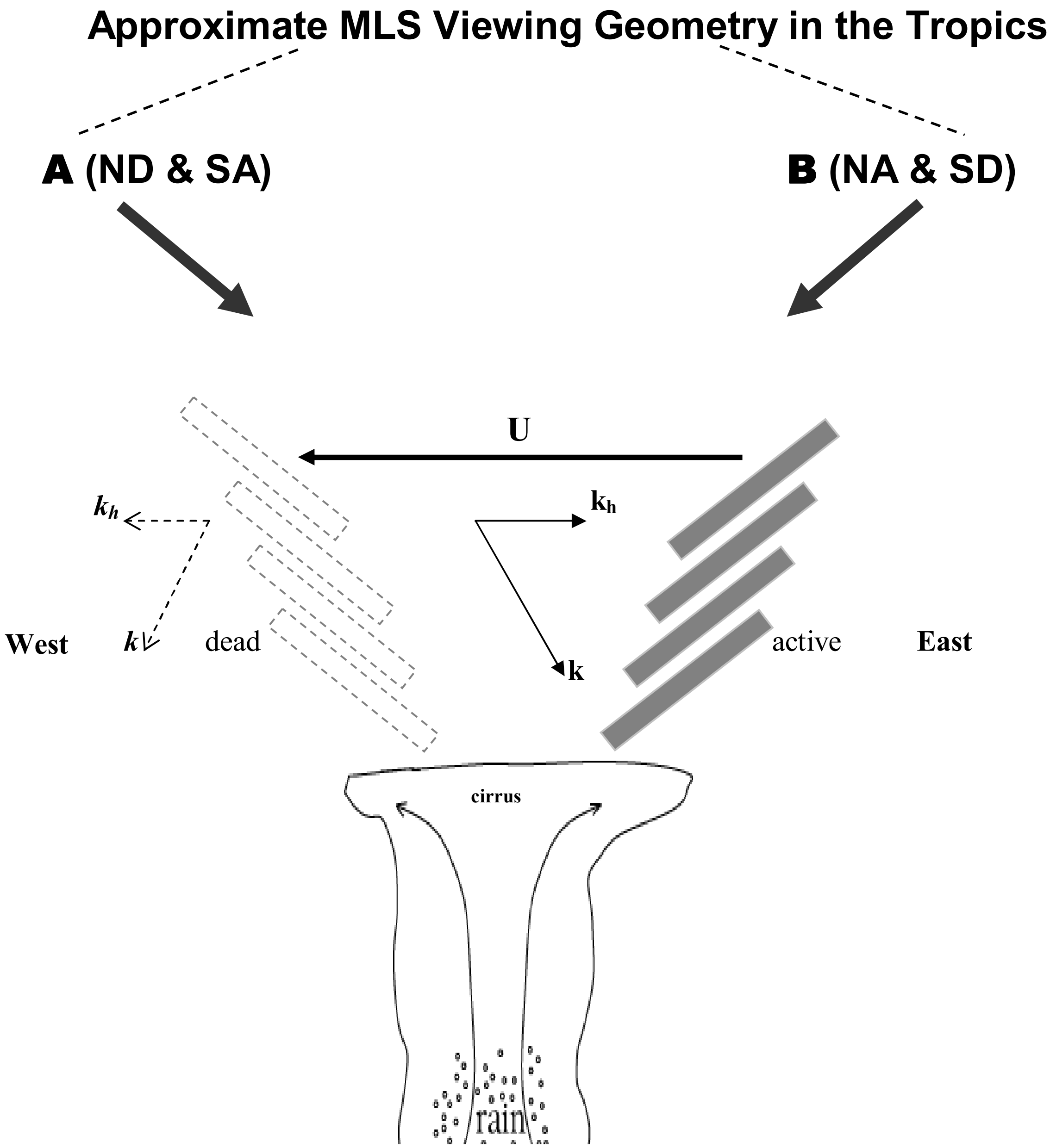

Figure 6: This Diagram shows the MLS inferred convection generated GW wave front propagation direction. Note only the wave fronts at "east half" of the convection have horizontal components of the wave vector $\mathbf{k_h}$ opposing the wind vector **U**. The other "west half" of the waves with $\mathbf{k_h}$ traveling in the same direction as **U** are "dead", or filtered out due to the "Doppler-shifting" effect on background winds. Two MLS viewing geometries are shown above the convective waves. Viewing geometry B is most favorable for resolving this wave perturbation in saturated MLS limb-scan radiances.

Figure 6

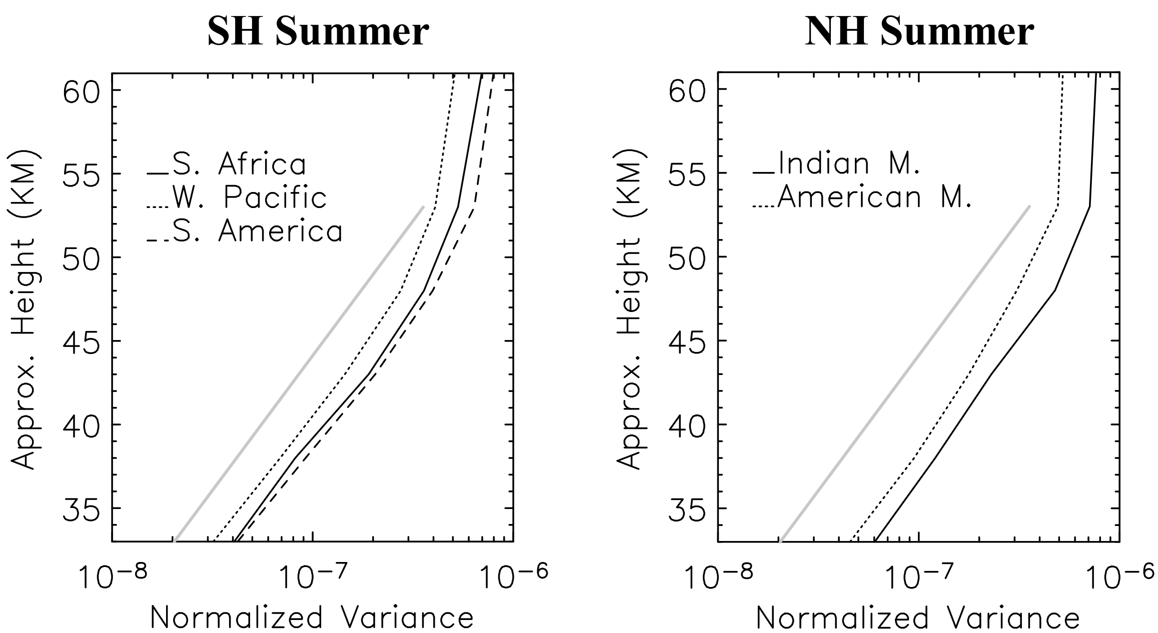

Figure 7: Vertical growth of normalized MLS GW mean variances over the major convections for Dec-Mar 1991-94 (left) and Jun-Sep 92-94 (right) as observed on NA and SD orbits. The instrument noise was removed from these variances. The grey curve shows sample $\exp\left(\int dz/H\right)$ growth with $H = 7\ km$.

Figure 7

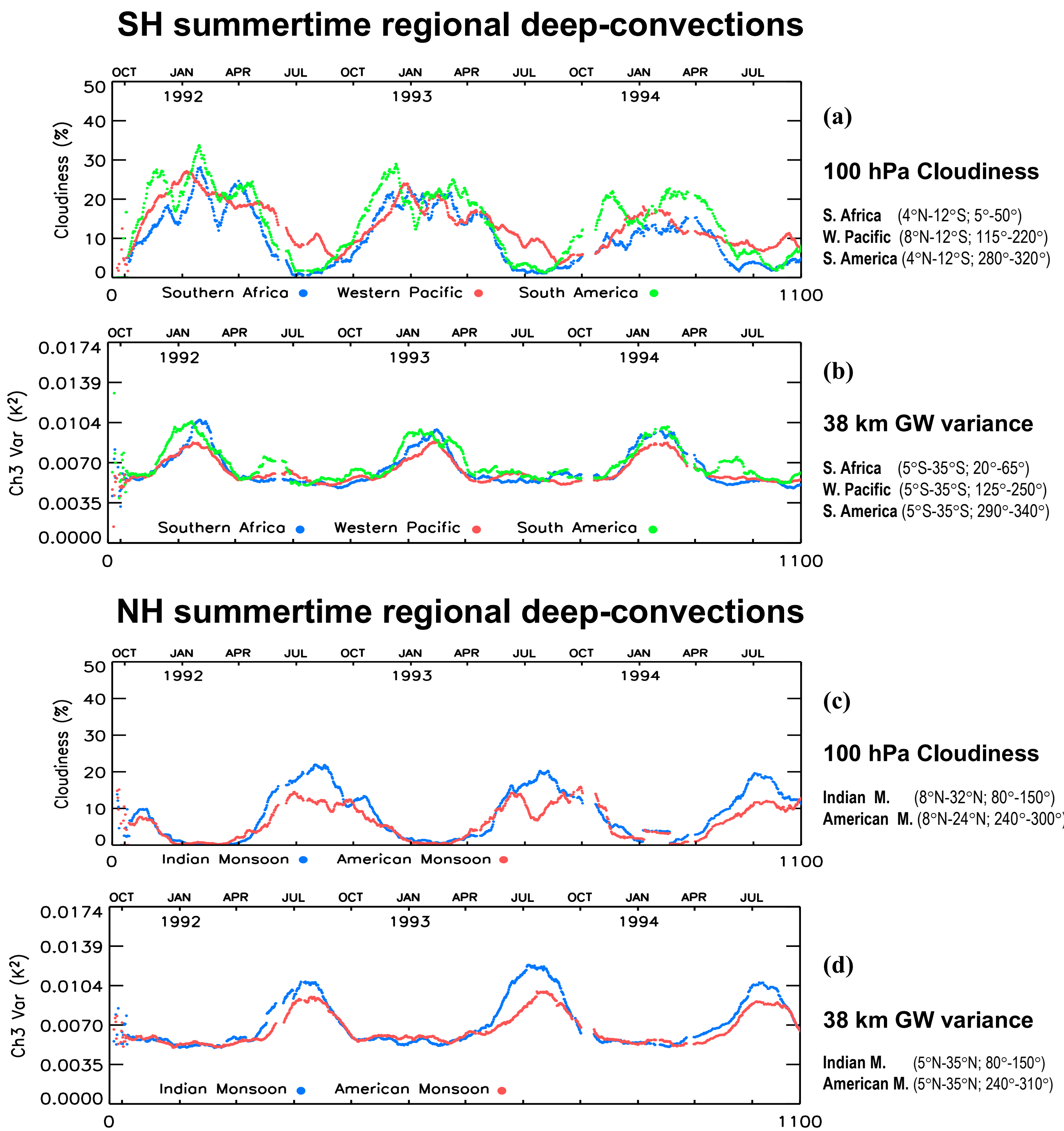

Figure 8: Time series of *100 hPa* cloudiness and *38 km* gravity wave variances above the most dominant regional convections, both are 30-day running window means of daily values. **(a)/(b):** Cloudiness and GW variance for three dominant NH winter-time convection regions of Southern Africa, Western Pacific, and South America; **(c)** and **(d)** Clounidess and GW variances for the two major NH summer-time convections, Indian Monsoon and American Monsoon. The latitudes and longitudes between the cloudiness and GW variances plots are slightly different for most of the convection regions, because the GW maxima are shifted following the stratosphere wind pattern as discussed in the text

Figure 8

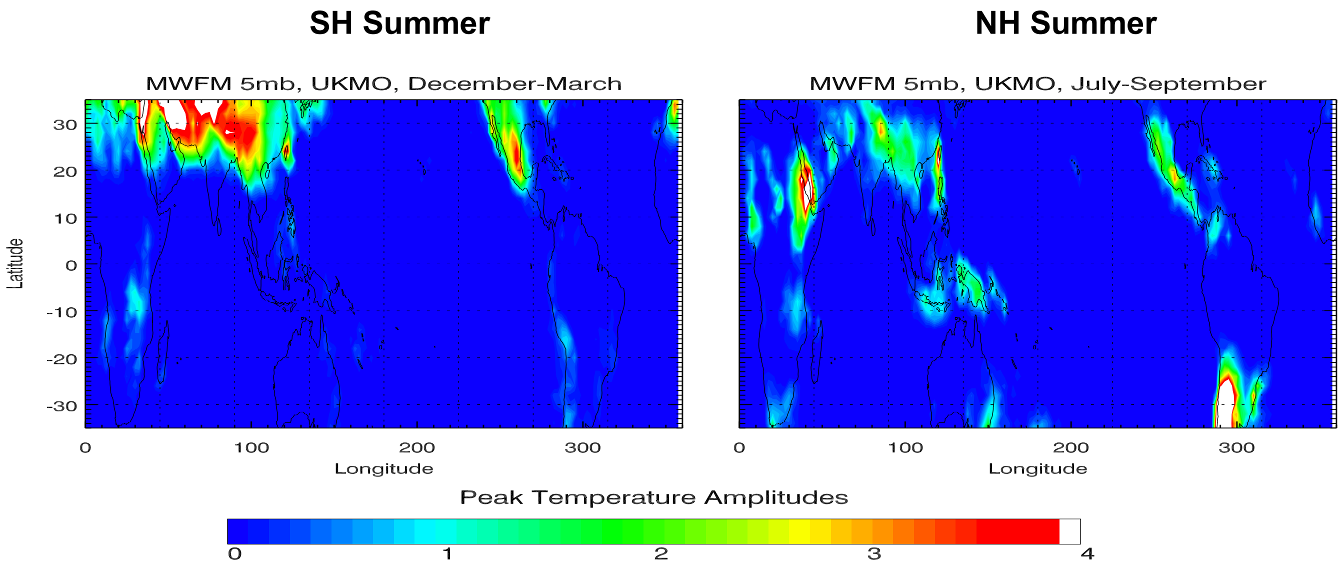

Figure 9: Left panel: NRL MWFM 2.1 simulated topography-related gravity waves for southern hemispheric summer (December-March 1991-92). Right panel: for northern hemisphere summer (July-September 1992). Results are averaged during the same MLS measurement days.

Figure 9

SH Summer **NH Summer**

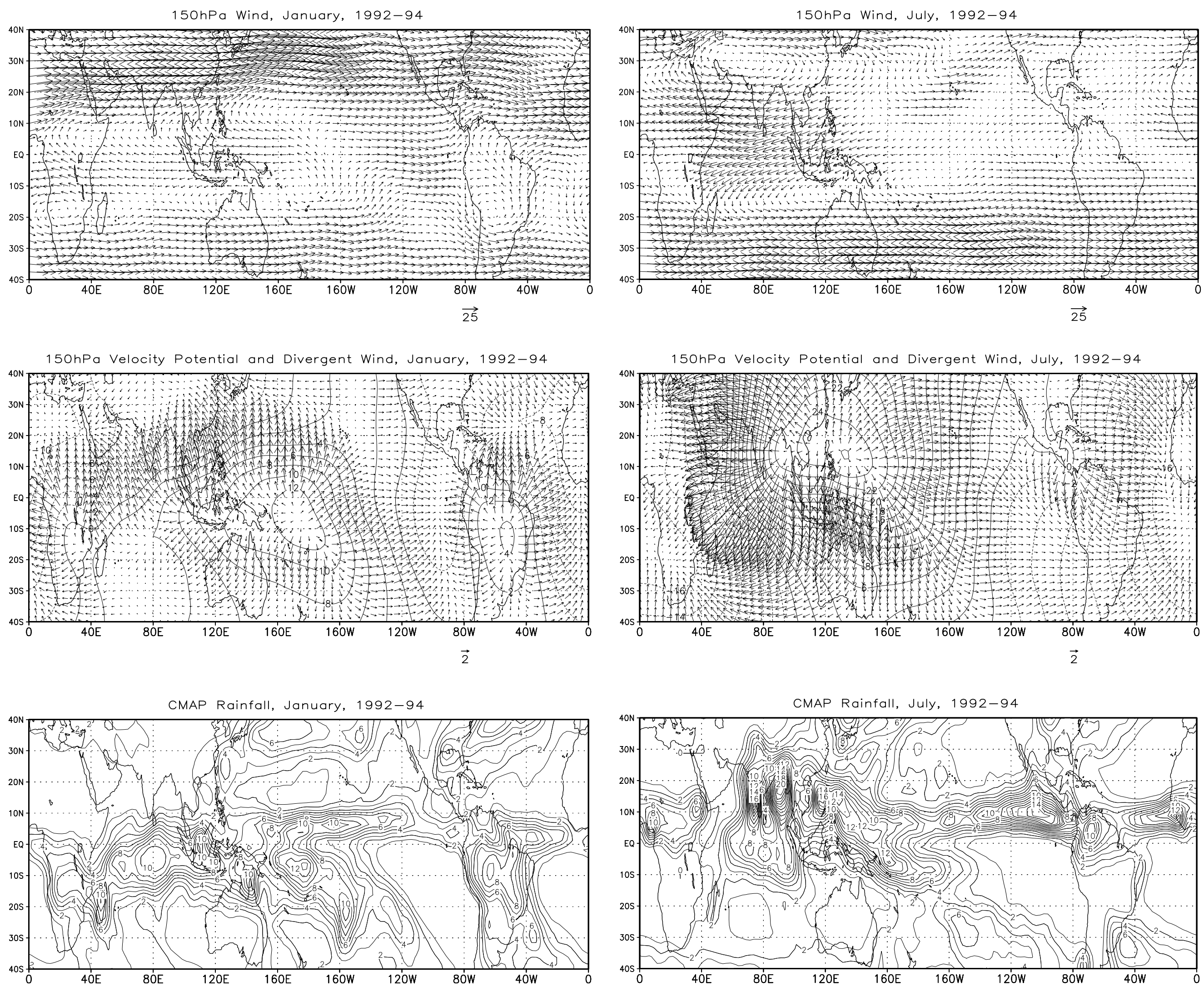

Figure 10: Left column: January 1992-94 mean 150-mb winds (top panel), velocity potential (interval $0.8{\times}10^{6}m^{2}s^{-1}$, dashed lines less than zero) and divergent winds (middle panel). Bottom panel is CMAP January mean rainfalls. Right column: As in left column except for July 1992-94 means.

Figure 10

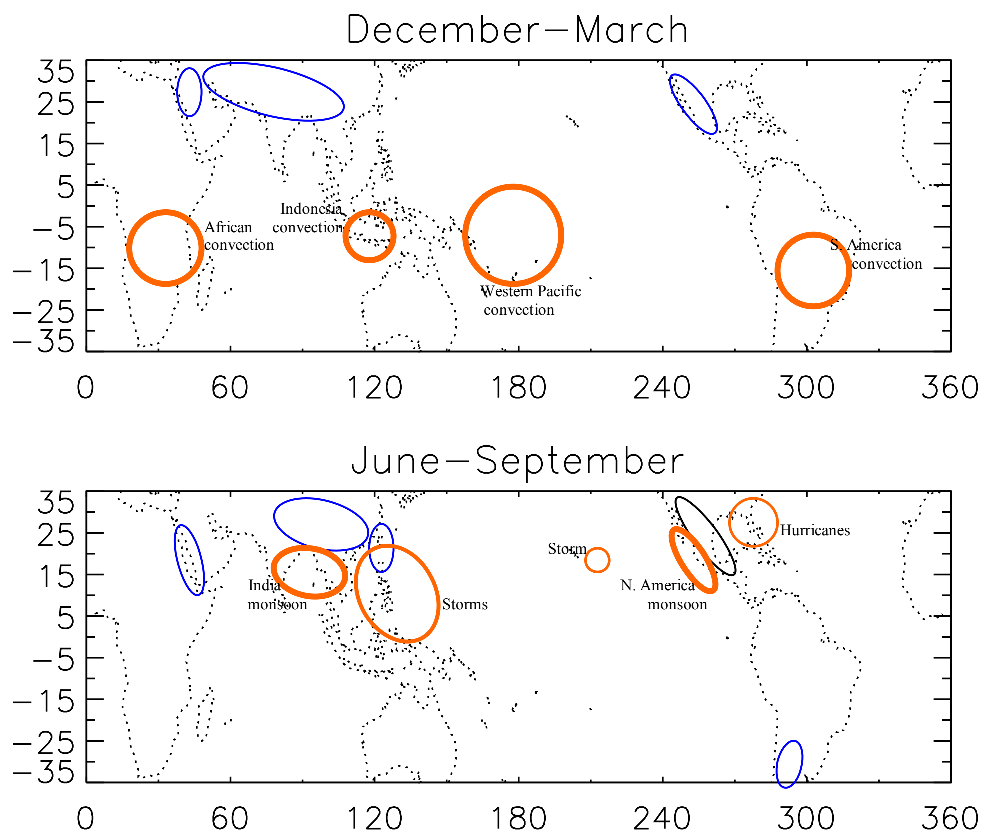

Figure 11: This simple diagram shows the regions of major deep-convection activities (red circles) and major topography related turbulences (blue circles).

Figure 11